

Spatiotemporally Controllable Electrical Stimulator via Independent Photobending and Upconversion Photoluminescence Using Two Different Wavelengths of Near-Infrared/Visible Light as Dual Stimuli

Jiyeon Lee, Dongjun Kim, Minsuk Park, Jaehyeok Ryu, Hyunbin Park, Taehee Kim, Dongho Kim, Sang-Yong Ju,* and Jiwon Kim*



Cite This: *ACS Appl. Mater. Interfaces* 2023, 15, 46311–46321



Read Online

ACCESS |

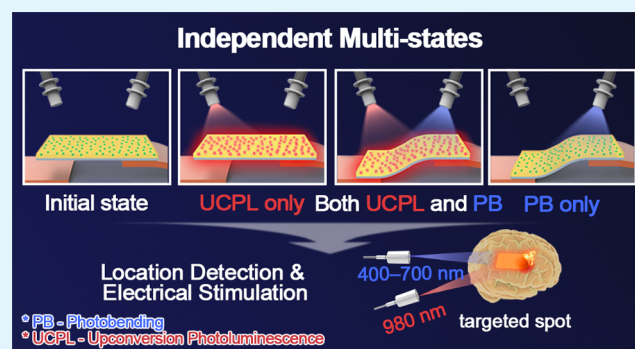
Metrics & More

Article Recommendations

Supporting Information

ABSTRACT: Multistimuli responsive materials are advantageous in that they can enhance the desired response or bypass unwanted reactions. Light is one of the most attractive stimuli since it allows remote spatiotemporal control and multiplexing of properties (e.g., wavelength, intensity, irradiation time, pulsed/continuous wave) for application on multiphotoresponsive materials. However, the operating wavelength for such photoresponsive systems often includes an ultraviolet (UV) range that limits its use in the biomedical field. Herein, we investigate near-infrared (NIR)/visible (Vis) light-responsive nanocomposite films composed of rare earth element (i.e., Yb, Er)-doped NaYF₄ nanoparticles (NPs) embedded in azobenzene-incorporated poly(dimethylsiloxane) (AzoPDMS), silk fibroin, and silver nanowire (AgNW) layers. Photobending (PB) of the nanocomposite film is induced by a Vis light of 400–700 nm, while upconversion photoluminescence (UCPL) of embedded NPs is activated by an NIR light of 980 nm. The excitation wavelength of photoluminescence (PL) is shifted to the NIR ($\lambda = 980$ nm) range via photon upconversion in rare earth element-doped NPs. Independent operation of PB and UCPL enables both on-demand electrical switching and real-time location monitoring for spatiotemporally controlled electrical pulse stimulation. As a result, the dual-photoresponsive nanocomposite film can be utilized as a remotely controllable electrical stimulator and location indicator via different wavelengths of light.

KEYWORDS: independent multistates, photoresponsive nanocomposite, photobending, upconversion photoluminescence, spatiotemporal control, electrical switch



1. INTRODUCTION

Stimuli-responsive materials show switching properties by applying a wide range of stimuli such as light,¹ chemical stimulation,² electromagnetic field,³ mechanical force,⁴ heat,⁵ or a combination of multiple stimuli.⁶ Specifically, multistimuli responsive materials have been actively studied in recent years since it can mimic complex systems and/or induce sequential reactions with enhanced performance compared to single-stimulus responsive materials.^{7–10} Advantages of using two or more stimuli have led to numerous fields of applications such as soft actuators,^{11–14} bioelectronics,^{15,16} and bioimaging.^{17,18}

Light is beneficial among various stimuli since it is noninvasive and spatiotemporally controllable. Moreover, light of various conditions (e.g., wavelength, intensity, irradiation time, pulse, continuous wave) can be applied as an independent stimulus and be multiplexed. Light-controlled multifunctional systems can be constructed by combining photoresponsive materials of optical, electrical, or mechanical reactions that operate with mechanisms of photoexcitation,

photoelectric effect, or photoisomerization, respectively. Through the utilization of different photoresponsive properties, a dual-photoresponsive nanocomposite was employed to create binary logic gates,¹⁹ optical encoding,²⁰ and chemical sensing.²¹

However, multiphotoresponsive materials encounter a few challenges when applied to bioelectronics. First, the wavelength range of the light for stimuli should be carefully selected so that they do not overlap nor interfere with each other to trigger each response without cross-talk. Second, near-infrared (NIR) light can penetrate tissues more deeply with less

Received: June 19, 2023

Accepted: August 29, 2023

Published: September 10, 2023



damage compared to ultraviolet (UV) light due to its longer wavelength.

Therefore, NIR light has been utilized as a stimulus by introducing 980 nm-absorbing sensitizers (e.g., Yb³⁺) into nanomaterials.²² Moreover, an appropriate emitter ion (e.g., Er³⁺) allows the conversion of multiple 980 nm photons transferred from the sensitizer ion to a photon of the Vis range. Particularly, doping two or more rare earth elements (e.g., Yb, Er) into nanoparticles (NPs) can convert NIR light (980 nm) to Vis range (e.g., 520, 541, and 655 nm) via photon energy transfer between the rare earth elements. For instance, codoping rare earth elements on single (e.g., Yb³⁺/Er³⁺ or Yb³⁺/Tm³⁺-doped NaYF₄ NPs^{23–25} or Yb³⁺/Er³⁺-doped RuPbI₃ perovskite nanowires²⁶) or multiple nanomaterial (e.g., Yb³⁺/Tm³⁺-doped NaYF₄ NPs coexisted with CsPbX₃ [X = Cl, Br, I] perovskite quantum dots (PQDs)²⁷) showed emission within the Vis range upon NIR light (980 nm) irradiation.

Herein, we developed a dual-photoresponsive spatiotemporal switch using nanocomposite films that can electrically stimulate and monitor the location simultaneously based on four independent states via a combination of Vis (400–700 nm) and NIR (980 nm) lights. Photoresponsive nanocomposite films can independently change their morphology and luminescence through three layers: NaYF₄ NPs doped with rare earth elements (Yb³⁺, Er³⁺) covered with a NaLuF₄ shell, which are embedded in AzoPDMS, silk fibroin, and silver nanowire (AgNW) layers. The difference in volume changes between AzoPDMS and silk fibroin upon Vis light irradiation induces structural changes in the nanocomposite film, which results in the bending of the film (photobending; PB), whereas NaYF₄:Yb,Er core-NaLuF₄ shell NPs emit a Vis light of specific wavelength via upconversion luminescence (UCPL) upon NIR light irradiation. Accordingly, PB and UCPL of the nanocomposite film can be independently operated by different wavelengths of light. Electrical pulse stimulation with precise spatiotemporal control is achieved by electrical switching via PB and light emission of UCPL; PB provides soft and repetitive stimulation to desired local areas, while UCPL allows us to locate the position of the film. Our nanocomposite film which exhibits multistates of bending and luminescence will be advantageous in developing optoelectronic devices for biomedical treatments.

2. EXPERIMENTAL SECTION

2.1. Materials. 4-Methoxy aniline, 6-bromo-1-hexene, chloroplatinic acid hexahydrate, magnesium sulfate, 1-octadecene (ODE, 90%), sodium hydride, ammonium fluoride, and sodium oleate (NaOA, ≥82% (fatty acids)) were purchased from Sigma Aldrich. Erbium(III) acetate tetrahydrate (99.9%) and lutetium(III) acetate hydrate (99.9%) were purchased from Alfa Aesar. Petroleum ether (90%), *n*-hexane (95%), phenol, and sodium hydroxide were obtained from Daejung. Silk fibroin (5% solution) was purchased from Advanced BioMatrix. Silver nanowire (1.0 wt %, dispersed in isopropyl alcohol) was obtained from Nanopyxis Ltd., Korea. A photoresist AZ-5214E was purchased from Microchemicals. Silicone elastomer base [poly(dimethylsiloxane) (PDMS) prepolymer] and silicone elastomer curing agent (Sylgard 184) were obtained from Dow Corning.

2.2. Synthesis of AzoPDMS. 1-(4-(Hex-5-enyloxy)phenyl)-2-phenyldiazene-incorporated poly(dimethylsiloxane) (AzoPDMS) was synthesized by the previously reported method.²⁸ The PDMS prepolymer and curing agent from a Sylgard 184 silicone elastomer kit were used. Chloroplatinic acid hexahydrate was added as a catalyst to graft the hexyloxy side chain of 1-(4-(hex-5-enyloxy)phenyl)-2-phenyldiazene with an alkene group to the PDMS backbone.

2.3. Synthesis of NaYF₄:Yb,Er Core-NaLuF₄ Shell NPs. NaYF₄:Yb,Er core-NaLuF₄ shell NPs were synthesized by a previously reported method: robust binary sodium strategy.²⁵ NaYF₄:Yb,Er (98/2%) core NPs were synthesized with ODE as a solvent under an argon environment. 2.94 mmol of Yb(CH₃COO)₃·3H₂O and 0.06 mmol of Er(CH₃COO)₃·3H₂O were used as reagents. The as-synthesized NaYF₄:Yb,Er NPs were purified with ethanol and dispersed in cyclohexane. Core NPs were added to 3.00 mmol of Lu(CH₃COO)₃·3H₂O dissolved in the ODE for shell synthesis. As-prepared core-shell NPs were washed with ethanol and dispersed in cyclohexane to obtain colloidal NaYF₄:Yb,Er core-NaLuF₄ shell NPs.

2.4. Synthesis of the NaYF₄:Yb,Er Core-NaLuF₄ Shell NP@AzoPDMS/Silk Fibroin/AgNW Trilayer Film. To fabricate the photoresponsive nanocomposite film, photoresist was initially spin-coated onto a Si wafer at 4000 rpm for 30 s and cured at 120 °C for 2 min. Then, silk fibroin solution was drop-cast onto the photoresist layer and dried for 12 h. NaYF₄:Yb,Er core-NaLuF₄ shell NP@AzoPDMS prepolymer solution with the curing agent was then spin-coated onto the silk fibroin layer and cured for cross-linking. In order to synthesize nanocomposite of rare earth element-doped NaYF₄ NPs and AzoPDMS, 0.4 mL of synthesized NaYF₄:Yb,Er core-NaLuF₄ shell NP dispersion (NP concentration: ~1.710 × 10¹⁵ mL⁻¹) was added dropwise to 1 g of as-prepared AzoPDMS prepolymer under stirring. 0.1 g of the silicone elastomer curing agent was added as a cross-linker and degassed in a desiccator for several hours. Afterward, NaYF₄:Yb,Er core-NaLuF₄ shell NP@AzoPDMS was spin-coated on a silk fibroin film at 2000 rpm for 1 min. The film was cured at 80 °C for 24 h, forming an AzoPDMS/silk fibroin bilayer film. The free-standing film was obtained by removing the photoresist with acetone, and diluted silver nanowire (AgNW) dispersion (0.1 wt %) was drop-cast onto the silk fibroin side of the film. After drying for 10 min, the film was used for further experiments.

2.5. Characterization. Ultraviolet–visible (UV–vis) absorption spectra were obtained from a UV–vis spectrometer (Lambda 365, PerkinElmer, Inc.). Photoluminescence (PL) spectra were measured using fluorescence spectrometers F-7100 (Hitachi Ltd.) for visible (Vis) ranges and SPEX Nanolog 3-211 (Horiba Scientific) for near-infrared (NIR) ranges with a 10 mm beampath quartz cuvette. An NIR-spectrometer equipped with a spectrometer (iHR 320) and an InGaAs array detector (Symphony II) was used to analyze the PL signal. Scanning electron microscopy (SEM) images were obtained using a JSM-7100F (JEOL Ltd.). High-resolution transmission electron microscopy (HRTEM) and energy dispersive spectroscopy (EDS) images were obtained using a JEM-ARM200F “NEO ARM” (JEOL Ltd.) and JED-2300T (Dual) (JEOL Ltd.), respectively. X-ray diffraction (XRD) was measured using a SmartLab X-ray diffractometer (Rigaku Corp.) with Cu K α radiation. ¹H nuclear magnetic resonance (NMR) spectra were obtained from an Agilent 400-MR NMR spectrometer (400 MHz for ¹H) with deuterated chloroform (CDCl₃) as a solvent and tetramethylsilane (TMS) as an internal standard, in which the chemical shifts are shown in parts per million (ppm). The spin coating processes were performed using a spin coater WS-650-23B (Laurell Technologies Corp.). Trace metal analysis was carried out using an inductively coupled plasma-mass spectrometer (ICP-MS, Agilent 7900).

2.6. Measurement of PB and UCPL. Xenon research arc lamp source (66924-450XV-R1, Newport Corp.) with a pump power of 450 W was used for light irradiation. For the photobending (PB) of nanocomposite films with Vis light, the 400–694 nm bandpass filter (BrightLine FF02-694/SP, Semrock) was equipped with the arc lamp. Using a laser power meter (Nova II, Ophir Optronics Solution Ltd.) coupled with a power sensor (PD300R-UV, Ophir Optronics Solution Ltd.), the output power of the arc lamp ($\lambda = 200–2500$ nm) was determined as 247.6 mW, whereas that of the arc lamp with the 400–694 nm bandpass filter was 51.12 mW. The lamp was housed in a dark Faraday cage with ice-based thermal circulation to eliminate effects of external electromagnetic fields and minimize thermal effects on the film, respectively. A circular light source with a diameter of 10 mm was used, and the distance from the light source to the film was 50 mm. A 980 nm diode laser (MDL-III-980-2W, CNI laser) with a

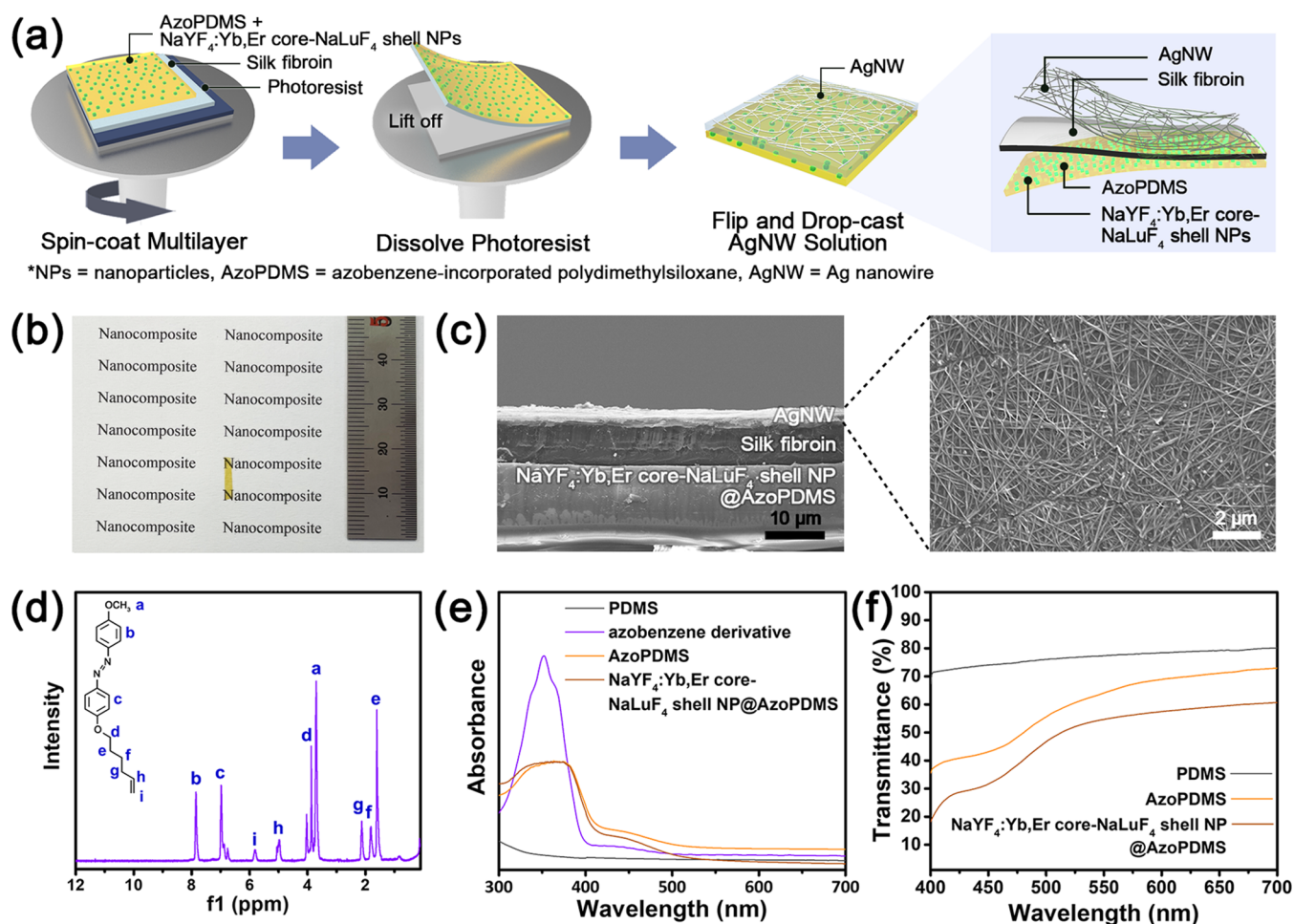


Figure 1. Fabrication, structure, and characterization of the NaYF₄:Yb,Er core-NaLuF₄ shell NP@AzoPDMS/silk fibroin/AgNW nanocomposite film. (a) Fabrication scheme and (b) optical image of NaYF₄:Yb,Er core-NaLuF₄ shell NP@AzoPDMS/silk fibroin/AgNW nanocomposite film. (c) Scanning electron microscopy (SEM) cross-sectional image of NaYF₄:Yb,Er core-NaLuF₄ shell NP@AzoPDMS/silk fibroin/AgNW nanocomposite film (left) and SEM front image of the AgNW layer (right). (d) Nuclear magnetic resonance (NMR) spectrum of 1-(4-(hex-5-enyloxy)phenyl)-2-phenyldiazene (azobenzene derivative). (e) Ultraviolet–visible (UV–vis) absorption spectra of PDMS, azobenzene derivative, AzoPDMS, and NaYF₄:Yb,Er core-NaLuF₄ shell NP@AzoPDMS nanocomposite film. (f) Transmittance spectra of PDMS, AzoPDMS, and NaYF₄:Yb,Er core-NaLuF₄ shell NP@AzoPDMS nanocomposite film.

power of 1 W was applied to the upconverting nanoparticles within the nanocomposite film for NIR irradiation.

2.7. Electrical Switching Test. Electrical measurements were performed using a Keithley 6517B (Keithley Inst.) electrometer with an applied voltage of 1 V, in which the data were collected in real-time with a Python code. In order to demonstrate the electrical switching process, two distinct copper electrodes connected to the electrometer were installed on both a brain model and a nose model. The nanocomposite film was attached to one of the copper electrodes with a silver paste.

3. RESULTS AND DISCUSSION

In order to develop a spatiotemporal electrical switch that independently exhibits photobending (PB) and upconversion photoluminescence (UCPL) upon visible (Vis) and near-infrared (NIR) light, respectively, we have designed a nanocomposite film in which photoluminescent nanoparticles (NPs) are embedded within a photoresponsive polymer, azobenzene-incorporated poly(dimethylsiloxane) (AzoPDMS). More specifically, the nanocomposite film consists of three layers; NaYF₄:Yb,Er core-NaLuF₄ shell NPs embedded in the AzoPDMS photoresponsive layer, silk fibroin supporting layer, and silver nanowire (AgNW) conductive layer. The trilayer

nanocomposite film is synthesized by the fabrication process described in Figure 1a. Photoresist is spin-coated on a silicon wafer, and silk fibroin is drop-cast onto the photoresist layer. Then, NaYF₄:Yb,Er core-NaLuF₄ shell NP@AzoPDMS is spin-coated onto the silk fibroin layer, followed by dissolving the photoresist and lifting off of the nanocomposite film. Finally, the AgNW dispersion is drop-cast onto the silk fibroin side of the film (more detailed processes are described in the Experimental Section). Of note, Y³⁺ sites of NaYF₄ are substituted with rare earth elements (i.e., Yb³⁺ and Er³⁺), which are hereinafter denoted as NaYF₄:Yb,Er NPs to effectively represent the doped elements despite the absence of Y³⁺. Also, NaYF₄:Yb,Er NPs were then covered with an optically inert NaLuF₄ shell (~2.5 nm) for stability and enhanced optical properties.

Following the fabrication processes, we obtained a free-standing NaYF₄:Yb,Er core-NaLuF₄ shell NP@AzoPDMS/silk fibroin/AgNW nanocomposite film. The nanocomposite film is flexible and transparent with a yellow tint, as shown in the optical image (Figure 1b). Also, a scanning electron microscopy (SEM) cross-sectional image of the whole film was acquired to confirm the structure of the nanocomposite

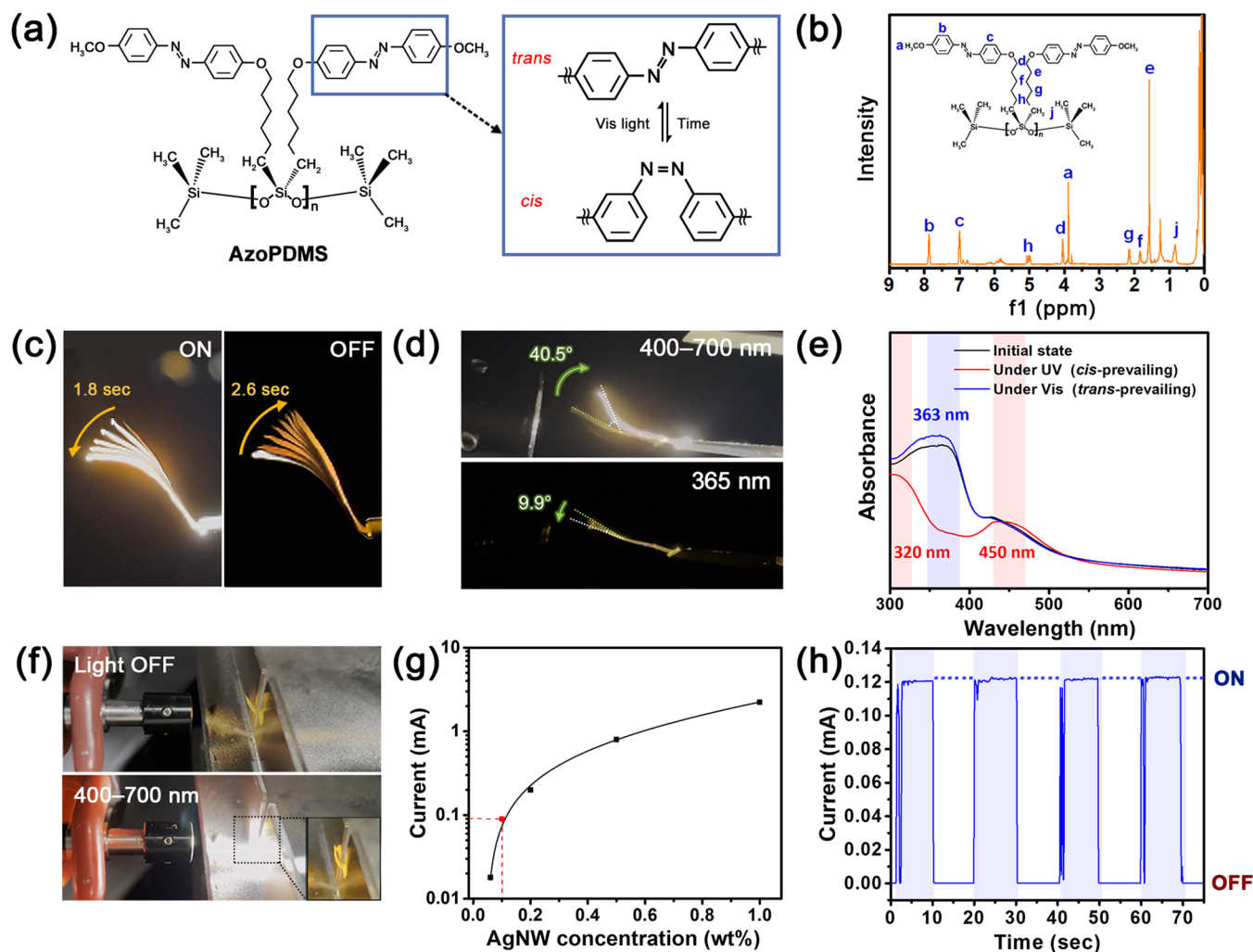


Figure 2. PB property and characterization of AzoPDMS in a nanocomposite film. (a) Chemical structure (left) and *cis*-*trans* isomerization (right) of AzoPDMS. (b) NMR spectrum of AzoPDMS. (c) Overlapped photographs of bending and stretching motions of NaYF₄:Yb,Er core-NaLuF₄ shell NP@AzoPDMS/silk fibroin/AgNW nanocomposite film upon 400–700 nm light irradiation (left panel; bending degree of 40.5° in 1.8 s) and in ambient condition with no irradiation (right panel; stretching in 2.6 s), respectively. (d) PB upon irradiation with 400–700 nm light (top; *cis* → *trans* transition) and 365 nm light (bottom; *trans* → *cis* transition). (e) UV-vis absorption spectrum of the AzoPDMS film and AzoPDMS prepolymer obtained upon irradiation with 365 nm and 400–700 nm. Peaks at 320 nm (π - π^* transition for *cis*-form) and 450 nm (n - π^* transition) correspond to the *cis*-isomer, while the peak at 363 nm (π - π^* transition for *trans*-form) corresponds to the *trans*-isomer. (f) Electrical switching setup of NaYF₄:Yb,Er core-NaLuF₄ shell NP@AzoPDMS/silk fibroin/AgNW nanocomposite film upon irradiation. Inset: close-up image of the film when irradiated with 400–700 nm light (image taken immediately after the light had been eliminated). (g) Electrical current flowing through the nanocomposite film that varies with the concentration of the AgNW dispersion. (h) Reversible ON/OFF current cycles of NaYF₄:Yb,Er core-NaLuF₄ shell NP@AzoPDMS/silk fibroin/AgNW with a duration of 20 s.

film (Figure 1c). The image shows a 10.09 μm thick NaYF₄:Yb,Er core-NaLuF₄ shell NP@AzoPDMS layer coated onto a 6.90 μm thick silk fibroin layer. SEM image of the AgNW layer was also obtained, presenting a densely connected random network of nanowires that would function as a single-sided conductive film.

The nuclear magnetic resonance (NMR) spectrum of 1-(4-(hex-5-enyloxy)phenyl)-2-phenyldiazene, hereinafter denoted as an azobenzene derivative, is given in Figure 1d and each peak was assigned to protons of the chemical structure in the inset. AzoPDMS is then synthesized via chemical bonding between alkene groups of an azobenzene derivative molecule and methyl groups of poly(dimethylsiloxane) (PDMS). To characterize optical properties of NaYF₄:Yb,Er core-NaLuF₄ shell NP@AzoPDMS/silk fibroin/AgNW nanocomposite film, absorption spectra of PDMS, azobenzene derivative,

AzoPDMS, and NaYF₄:Yb,Er core-NaLuF₄ shell NP@AzoPDMS nanocomposite film were obtained by ultraviolet-visible (UV-vis) spectrometry, as provided in Figure 1e. The wavelength of maximum absorbance (λ_{max}) for AzoPDMS was 363 nm, which was nearly the same as that of azobenzene derivative, while no peak was observed for PDMS. This indicates that the azobenzene derivative molecules are well incorporated within AzoPDMS, retaining its optical characteristics.²⁹ AzoPDMS and NaYF₄:Yb,Er core-NaLuF₄ shell NP@AzoPDMS nanocomposite films showed similarity in the configuration of absorption spectra. Transmittance of AzoPDMS and NaYF₄:Yb,Er core-NaLuF₄ shell NP@AzoPDMS nanocomposite film is also depicted in Figure 1f. AzoPDMS and NaYF₄:Yb,Er core-NaLuF₄ shell NP@AzoPDMS exhibited transmittances of ~64.1 and ~54.6%, respectively (at 550 nm, converted from UV-vis spectra),

indicating that the NPs tend to reduce the transmittance across the entire wavelength range.

The multiphotoreponsive nanocomposite film shows reversible PB and UCPL independently and simultaneously via irradiating two different wavelengths of light as dual stimuli. Four possible multiplexed states of 00₍₂₎, 01₍₂₎, 10₍₂₎, and 11₍₂₎ generated as the two binary states (i.e., PB and UCPL) were implemented, where the 00₍₂₎ state represents the initial state without any external stimulus applied.¹⁹ As a result, the abovementioned nanocomposite film can act as a spatiotemporally controllable electrical stimulator and location indicator in a light-accessible environment; PB of the film can function as an electrical stimulator upon Vis light irradiation, whereas UCPL can locate the film upon NIR light irradiation.

Synthesized AzoPDMS acts as a photoresponsive polymer inducing PB with silk fibroin as a supporting layer by 400–700 nm Vis light irradiation. The bilayer changes its shape upon irradiation owing to the difference in volume change of each layer via photoisomerization (Figure 2a). NMR spectrum of the synthesized AzoPDMS was obtained for structural characterization, and each peak was assigned to protons of the chemical structure in the inset as shown in Figure 2b.

The *cis*–*trans* isomerization of the incorporated azobenzene moieties induces a volume change in AzoPDMS, resulting in the bending of AzoPDMS and silk fibroin bilayer toward the silk fibroin side.²⁸ More precisely, irradiation with 400–500 nm light converts azobenzene moieties into its *trans*-form, increasing the volume of AzoPDMS.³⁰ Although it is less common, it might be attributed to the increase in steric hindrance between polymer chains.^{31,32} The intricate interplay of factors such as polymer packing/entanglement,³³ azobenzene attachment sites (side chain or backbone),³⁴ and the orientation/distribution of azobenzene entities can collectively influence volumetric changes, particularly in a macro-scale. In this study, we used the 400–700 nm wavelength range of Vis light using a BrightLine FF02-694/SP optical filter, which fully covers the abovementioned wavelength range.

NaYF₄:Yb,Er core-NaLuF₄ shell NP@AzoPDMS/silk fibroin/AgNW nanocomposite film shows the PB property as depicted in Figure 2c. When 400–700 nm light was irradiated, *trans*-form of AzoPDMS became dominant, which caused the film to bend in a direction where silk fibroin folded, as mentioned above. Nanocomposite film gradually bent up to 40.5° in 1.8 s upon 400–700 nm light irradiation (51.12 mW; measured by a laser power meter with the bandpass filter mounted on the lamp). When the light source was removed, the morphology of AzoPDMS was restored to its initial form, stretching back within 2.6 s. The delay in the response time of bent → stretched compared to stretched → bent is due to the difference in reaction time between *trans* → *cis* and *cis* → *trans* isomerizations in the AzoPDMS/silk fibroin bilayer.²⁸ Interestingly, AzoPDMS/silk fibroin bilayer can stretch not only by eliminating 400–700 nm light but also by irradiating 365 nm monochromatic light to cause *trans* → *cis* transition in the azobenzene moiety. Accordingly, PB occurred in the opposite direction upon 365 nm light irradiation, which indicates that 365 nm light accelerates *trans* → *cis* transition, resulting in the contraction of AzoPDMS (Figure 2d). In addition, we examined the PB stability of the nanocomposite film by cyclic bending/stretching fatigue testing, measuring the change in bending angle for each cycle. The nanocomposite film not only maintains its properties without exhaustion even

after 100 bending/stretching cycles but also retains the same PB performance even after a few days (Figure S1).

Although the isomer stability of azobenzene in the polymer is primarily determined by the polarity of dipole moment in the *trans*- and *cis*-forms,³⁵ other factors including van der Waals force,³⁶ hydrogen bonding,³⁷ molecular weight,³⁸ alignment of polymer,³⁹ and steric hindrance⁴⁰ are also known to have an effect. For instance, previous research on an azobenzene-based organic semiconductor polymer demonstrated that an equilibrium state of the film (condensed phase) comprises a combination of *trans*- and *cis*-forms due to steric hindrance in contrast to the dispersion in solution (liquid phase). Similarly, an initial state of the AzoPDMS layer in nanocomposite film can be in between *trans*- and *cis*-prevailing states (Figure 2e) compared to the AzoPDMS prepolymer (Figure S2); *trans*- or *cis*-prevailing states refer to the state in which the AzoPDMS layer receives substantial Vis or UV light (at least for 1 h), respectively, reaching the highest population of each isomer within the AzoPDMS layer. This observation suggests that the steric hindrance increased by cross-linking of the prepolymer may shift the isomerization equilibrium toward the *cis*-form of azobenzene.^{41,42} In particular, azobenzene moieties in the AzoPDMS film could be stacked without free space being in an intermediate state, whereas they are in *trans*-prevailing state when the AzoPDMS prepolymer is dispersed in solution as identified by UV–vis absorption spectra (Figure S2), time-resolved absorption (TA) spectra (Figure S3), and NMR spectra (Figure S4) (detailed explanations are also appended in the Supporting Information). This enables bidirectional photoisomerization (*trans*-to-initial and *cis*-to-initial states) and PB behavior (i.e., bending direction and degree, as shown in Figure 2d) of AzoPDMS via corresponding wavelengths of light. Previous works also reported that the *cis*-to-*trans* isomerization from the equilibrium state of azobenzene-incorporated polymers/aggregates can be induced by exposure to Vis light; (i) azobenzene-containing polymethacrylates exhibited the equilibrium state between *cis*- and *trans*-isomer caused by polymer alignment disruption due to the low anisometry of *cis*-azobenzene.³⁹ (ii) Azobenzene-based organic semiconductor polymer films demonstrated that equilibrium state-to-*trans* reaction occurred by steric hindrance in the condensed phase.⁴⁰ (iii) Azobenzene-functionalized alkane-thiol in aqueous solution exhibited higher *trans*-isomer concentration after Vis illumination due to aggregation compared to nonirradiated solution.⁴³

Moreover, an electrical switch was designed to observe the electrical performance of the photoresponsive multistitch. An electrical circuit was constructed by incorporating a copper electrode and an electrometer, and the film with a AgNW layer served as a flexible conductive electrode. Electrical ON/OFF states were operated by the bending/stretching of nanocomposite film with one side fixed on one electrode, while the other side was either in contact with (ON) or detached from (OFF) another electrode (Figure 2f). More precisely, the incorporated azobenzene moieties in the AzoPDMS layer of the nanocomposite film underwent *cis*-to-*trans* isomerization upon irradiation with 400–700 nm light, which induced a volumetric expansion of the AzoPDMS layer. Consequently, a volume discrepancy between photoresponsive (AzoPDMS) and supporting (silk fibroin) layers led the film to bend toward the silk fibroin layer bringing the film in contact with the other electrode. Since the AgNW layer was applied to the silk fibroin side of the nanocomposite film for an electrical contact, the

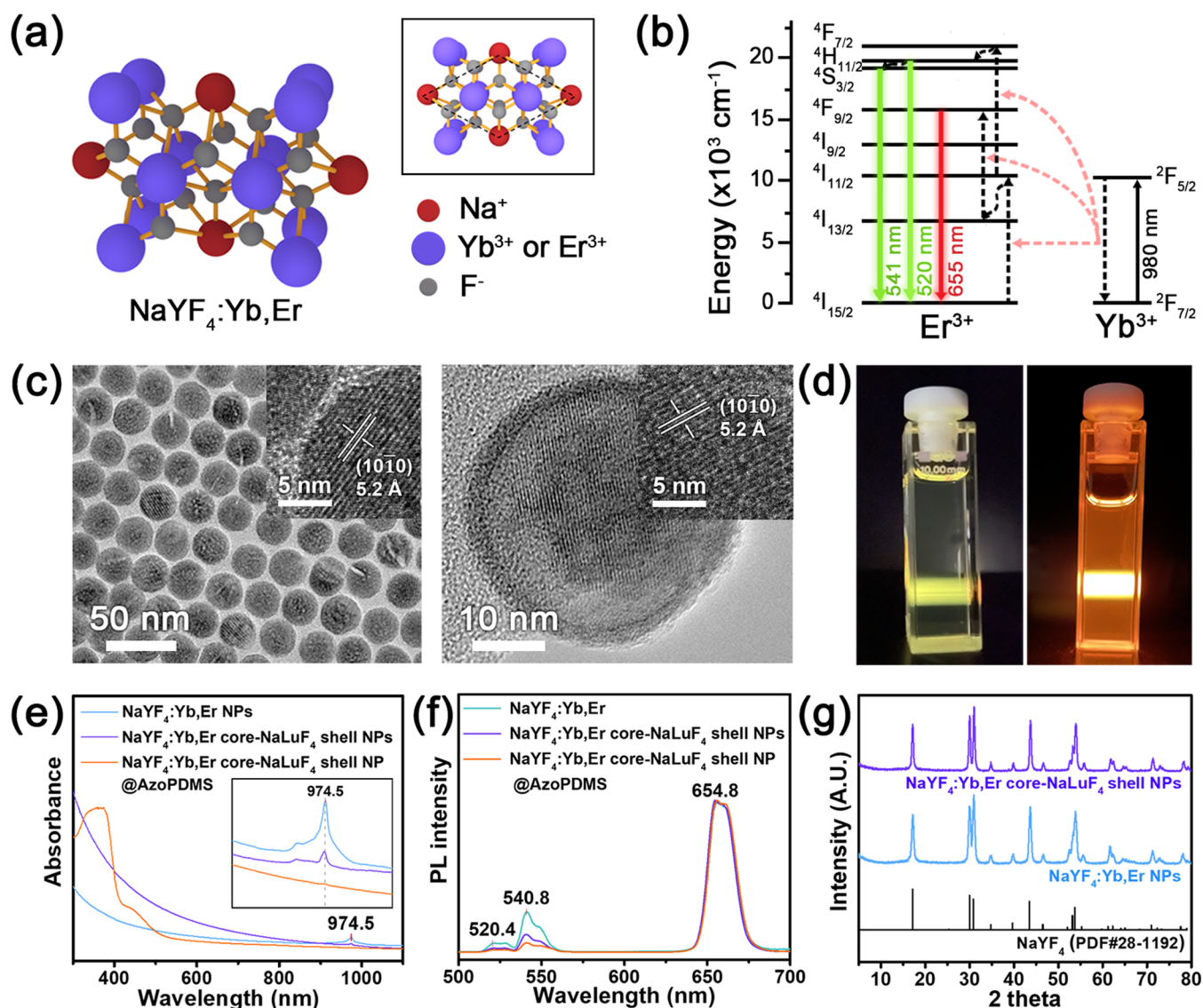


Figure 3. UCPL property and characterization of $\text{NaYF}_4:\text{Yb,Er}$ NPs in a nanocomposite film. (a) Crystal structure and (b) energy band structure with possible photon upconversion pathways of $\text{NaYF}_4:\text{Yb,Er}$. (c) Transmission electron microscopy (TEM) images and lattice parameters of $\text{NaYF}_4:\text{Yb,Er}$ NPs (left panel) and $\text{NaYF}_4:\text{Yb,Er}$ core- NaLuF_4 shell NPs (right panel). (d) Optical UCPL images of $\text{NaYF}_4:\text{Yb,Er}$ NPs (left panel) and $\text{NaYF}_4:\text{Yb,Er}$ core- NaLuF_4 shell NPs (right panel) upon 980 nm light irradiation. (e) Absorbance spectra and (f) PL spectra under 980 nm excitation of $\text{NaYF}_4:\text{Yb,Er}$ NPs, $\text{NaYF}_4:\text{Yb,Er}$ core- NaLuF_4 shell NPs, and $\text{NaYF}_4:\text{Yb,Er}$ core- NaLuF_4 shell NP@AzoPDMS nanocomposite film. Inset: magnified absorbance spectra with peaks close to 980 nm. (g) X-ray diffraction (XRD) patterns of $\text{NaYF}_4:\text{Yb,Er}$ NPs and $\text{NaYF}_4:\text{Yb,Er}$ core- NaLuF_4 shell NPs.

bending and stretching behavior of the nanocomposite film enabled the operation of electrical ON/OFF states, allowing remote control of electrical conductivity through photo-responsive property of the nanocomposite film.

The degree of electrical stimulation applied by conduction through AgNW dispersion, which is deposited onto the silk fibroin layer, is dependent on the connectivity of AgNWs as predicted by the percolation theory.⁴⁴ As the concentration of AgNWs increased, a denser and more interconnected network of AgNW is formed⁴⁵ (Figure 2g). By employing a 0.1 wt % diluted AgNW dispersion, we achieved a current flow of ~ 0.1 mA. The electrical circuit involving $\text{NaYF}_4:\text{Yb,Er}$ core- NaLuF_4 shell NP@AzoPDMS/silk fibroin/AgNW nanocomposite film showed multiple reversible ON/OFF cycles of conductance with a square wave (Figure 2h). Vis light was repetitively irradiated and eliminated for 10 s each, resulting in a cycle

duration of 20 s. The ON state was maintained for ~ 9.4 s, while the reaction times of OFF \rightarrow ON and ON \rightarrow OFF were 0.9 and 0.3 s, respectively. The OFF \rightarrow ON transition time was longer despite faster *cis* \rightarrow *trans* isomerization due to the actuation time required for physical contact between the nanocomposite film and the electrode.

$\text{NaYF}_4:\text{Yb,Er}$ NPs embedded in AzoPDMS allowed the film to emit light in the Vis range via UCPL when excited by 980 nm NIR light. $\text{NaYF}_4:\text{Yb,Er}$ NPs were utilized as luminescent NPs since the $\text{Yb}^{3+}\text{-Er}^{3+}$ ion pair is well-known to emit Vis (red and green) light upon 980 nm light irradiation by photon energy transfer.^{46,47} As illustrated in Figure 3a, $\text{NaYF}_4:\text{Yb,Er}$ NPs have a hexagonal structure, and Y^{3+} sites were fully substituted with 98% of Yb^{3+} and 2% of Er^{3+} ions for NIR-induced PL. The doping concentrations of Yb^{3+} and Er^{3+} were confirmed by inductively coupled plasma-mass spectrometry

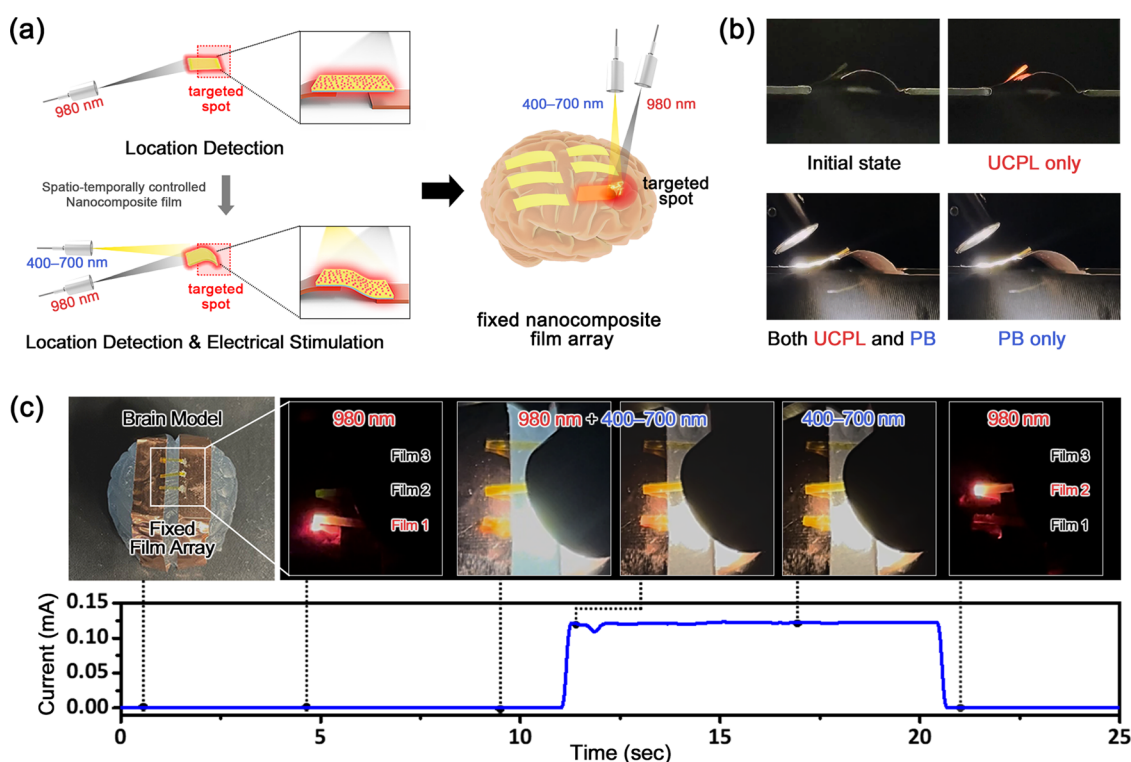


Figure 4. Spatiotemporal electrical switching action with independent multistates of NaYF₄:Yb,Er core-NaLuF₄ shell NP@AzoPDMS/silk fibroin/AgNW trilayer nanocomposite film upon Vis and NIR irradiation. (a) Schematic images of a nanocomposite film irradiated with 980 nm light (NIR for UCPL) to indicate the film's location and subsequently irradiated with 400–700 nm light (Vis for PB) for electrical stimulation, which is applied as a spatiotemporally controllable electrical stimulator demonstrated with fixed nanocomposite film array on a brain model. (b) Independent multistates of the nanocomposite film; “initial”, “UCPL-only”, “both UCPL and PB”, and “PB-only”. (c) The nanocomposite film operating in the sequential process of location monitoring and electrical stimulation via NIR/Vis irradiation by assembling a nanocomposite film array with an electrical circuit fixed on a brain model.

(ICP-MS) (Table S1) and transmission electron microscopy-energy dispersive spectroscopy (TEM-EDS) (Figure S5). Note, NaLuF₄, which has the same or smaller lattice spacing than NaYbF₄ or NaErF₄, was adopted as the optically inert shell material since the shell grows conformally only when a tensile structure is formed.⁴⁸ Doped Yb³⁺ ions absorbed 980 nm light and transferred the corresponding energy to the upper electronic states of Er³⁺ ions through various routes. Therefore, NaYF₄:Yb,Er NPs exhibited UCPL (anti-Stokes shift), radiating specific wavelengths of light in the Vis region: 520, 541, and 655 nm upon 980 nm light irradiation, with peaks corresponding to ⁴H_{11/2}–⁴I_{15/2}, ⁴S_{3/2}–⁴I_{15/2}, and ⁴F_{9/2}–⁴I_{15/2} energy transfer in Er³⁺ ions, respectively (Figure 3b).⁴⁹

Figure 3c shows TEM images of as-prepared upconverting nanoparticles (UCNPs): NaYF₄:Yb,Er NPs and NaYF₄:Yb,Er core-NaLuF₄ shell NPs. The size of NaYF₄:Yb,Er NPs was 24.4 ± 0.7 nm, while that of NaYF₄:Yb,Er core-NaLuF₄ shell NPs was 31.9 ± 3.4 nm with a shell thickness of ~2.5 nm. To note, the intermixing of core and shell in NaYF₄ host material can occur as the core particles release ions during shell growth due to their solubility.⁵⁰ Lattice parameters of each particle obtained in higher magnified TEM images were both 5.2 Å, which matched well with the (10 $\bar{1}$ 0) plane. NaYF₄:Yb,Er NPs and NaYF₄:Yb,Er core-NaLuF₄ shell NPs dispersed in cyclohexane produced noticeable UCPL upon 980 nm light irradiation (Figure 3d). Absorption and emission properties on account of doping elements were characterized by UV–vis and PL spectra, respectively. UV–vis spectra of both NaYF₄:Yb,Er NPs and NaYF₄:Yb,Er core-NaLuF₄ shell NPs showed

absorbance peaks close to 980 nm (Figure 3e). Meanwhile, the NaYF₄:Yb,Er core-NaLuF₄ shell NP@AzoPDMS nanocomposite film exhibited insignificant absorption near 980 nm owing to the UV–vis light beam traveling through fewer proportions of NPs compared to the NP dispersion. In detail, NP concentration of the NP dispersion is ~1.710 × 10¹⁵ mL⁻¹ with a cuvette path length of 10 mm, while that of NaYF₄:Yb,Er core-NaLuF₄ shell NP@AzoPDMS nanocomposite film is ~6.598 × 10¹⁴ mL⁻¹ with an AzoPDMS thickness of 10.09 μm, resulting in a ratio of NPs in nanocomposite film and NP dispersion within the beampath to be ~1/2500 (the detailed particle concentration estimation is described in pages 10 and 11 of the Supporting Information).

However, the nanocomposite film clearly showed UCPL upon 980 nm light irradiation, indicating that a lower concentration of NP is sufficient for light emission as explained below. Photoexcitation of NaYF₄:Yb,Er NPs, NaYF₄:Yb,Er core-NaLuF₄ shell NPs, and NaYF₄:Yb,Er core-NaLuF₄ shell NP@AzoPDMS nanocomposite film upon 980 nm light irradiation resulted in PL spectra with peaks at 520, 541, and 655 nm (Figure 3f). The spectra were normalized by the intensity of the 655 nm emission peak. NaYF₄:Yb,Er core-NaLuF₄ shell NPs showed enhanced luminescence compared to that of core-only NaYF₄:Yb,Er NPs since surface defects causing fluorescence quenching might be reduced by the NaLuF₄ shell. The intensity ratio of red (655 nm) to green (520, 541 nm) increased after the introduction of NaLuF₄ shell to NaYF₄:Yb,Er NPs, as previously reported.⁵¹ XRD patterns of NaYF₄:Yb,Er NPs and NaYF₄:Yb,Er core-NaLuF₄ shell NPs

were also obtained with hexagonal β -NaYF₄ (PDF #28-1192) as a reference (Figure 3g). XRD data confirmed that NaYF₄:Yb,Er NPs and NaYF₄:Yb,Er core-NaLuF₄ shell NPs were grown in hexagonal structures since peaks observed at 17.1, 30.0, 30.8, 34.7, 39.7, 43.5, 46.5, 52.1, 53.2, and 53.7° correspond to the (100), (110), (101), (200), (111), (201), (210), (002), (300), and (211) planes, respectively.

Our nanocomposite film composed of polymer-based trilayer with luminescent NPs can function as a spatiotemporally controllable electrical switch; the film with UCPL by NIR light irradiation enables us to monitor the location of the film in real-time, while the morphological change of the targeted film via PB facilitates electrical switching upon Vis light irradiation. Consequently, the film provides electrical switching at the intended location with desired conditions (e.g., frequency, pulse duration, operation time) via spatiotemporally controlled UCPL and PB. The targeted location was determined in real-time using 980 nm light, followed by the onset of electrical switch using 400–700 nm light (Figure 4a).

Independent multistates of initial, UCPL-only, both UCPL and PB, and PB-only were performed to verify the real-time operation of both location monitoring and electrical stimulation (Figure 4b). UCPL and PB processes are independent of each other's stimulating light wavelengths as demonstrated in Figure S6; 400–700 nm light irradiation for PB did not induce any PL emission, while irradiation with 980 nm light used for UCPL did not cause PB. Importantly, the excitation light power of each stimulus can be varied to control the bending degree of PB and emission intensity of UCPL (Figure S7).

The independent operation of UCPL and PB can facilitate complex functions involving location detection, followed by electrical stimulation. This functionality is beneficial in systems with limited visibility and restricted accessibility (e.g., nervous tissue in the brain/spinal cord/nerves, or muscle tissue in the walls of the hollow visceral organs/skeleton) that require spatiotemporally precise and finely controlled electrical stimulation, particularly narrow and wrinkled surfaces where it is difficult to appositely conform and apply electrical stimulation with rigid electrodes. Here, we demonstrated practical applications of our spatiotemporal electrical switch by assembling nanocomposite films onto electrical circuits on a brain model that exhibits sequential location detection and electrical stimulation.

Therefore, the electrical stimulation process by the spatiotemporal switch with a film array of three films (Film 1, 2, and 3) was demonstrated on a brain model in real-time where each state lasted for 5 s (Figure 4c); (i) an initial state with no irradiation was observed, (ii) followed by 980 nm light irradiation to detect UCPL, (iii) then 400–700 nm light was added for simultaneous UCPL and PB, and (iv) 980 nm light was removed for the final 5 s to display the PB-only state. A video of the full process is available in the Supporting Information (Video S1). Also, the three films, which are connected to separate electrodes exhibited independent properties of UCPL and PB with its corresponding current signal (in the range of 0.1 mA), indicating the selective stimulation performance (Figure S8). The location of the targeted film among a film array was identified by UCPL upon 980 nm irradiation, which could be observed with the naked eye by its red photoluminescence. This is advantageous not only for targeted stimulation but also for stimulation with high spatial selectivity and precise simultaneous control. Imple-

mentation of optical filters may enhance the intensity difference between fluorescence and background light, allowing more accurate identification.⁵² Furthermore, the bending and stretching of the electrical switch with the corresponding current signal acted as an electrical stimulator. The delays in OFF → ON (1.2 s) and ON → OFF (0.7 s) states are due to the required actuation time as explained in Figure 2h. Our nanocomposite switch is capable of repetitive electrical pulse stimulation at a low frequency (~0.53 Hz; calculated by the response time in Figure 4c), making it compatible with nervous system treatment (the noradrenergic system responds to 0.1–4 Hz stimulation⁵³).

Furthermore, identification and stimulation of the film at the desired position can be accomplished not only by identifying the location of the fixed film array under a moving light source but also by locating the film that reached the target position under a fixed light source at the desired location (Figure S9a). The latter can be employed for treatments in which electricity is applied to the targeted spot (e.g., nasal electrocautery), as demonstrated in Figure S9b and Video S2. This not only allows precise positioning within a narrow and tortuous tube but also minimizes unintended stimulation owing to the one-sided conductivity of our nanocomposite film.

These prototypes illustrate the mobility of either film or light source, expanding the degree of spatial and temporal freedom by utilizing light as a stimulus. They could further be applied for practical uses by down-scaling the films and arranging them into a flexible microarray patch for high-resolution wound treatment^{54,55} with high spatial accuracy. Moreover, owing to the tissue penetrating properties of NIR light, an application of the nanocomposite film can be extended by converting the azobenzene moiety of AzoPDMS into photoswitchable molecules that absorb NIR either directly⁵⁶ or indirectly with the assistance of UCNPs.⁵⁷

In summary, our spatiotemporal electrical switch can facilitate its application as a low-frequency electrical stimulator in conjunction with a real-time location indicator in a light-accessible environment, providing precise and remote control of electrical stimulation by PB and device positioning by UCPL at the same time. We believe our work will be beneficial for precisely controlled electrosurgical treatments since the switch can be remotely controlled, and the embedded luminescent nanomaterials ensure positional accuracy.

4. CONCLUSIONS

In this study, a novel multiphotoreponsive nanocomposite electrical switch consisting of photoresponsive polymer (AzoPDMS) and upconverting luminescent nanoparticles (NaYF₄:Yb,Er core-NaLuF₄ shell NPs) was developed. ON/OFF electrical switch motion controlled by photobending (PB) and real-time position tracking enabled by upconversion photoluminescence (UCPL) of NaYF₄:Yb,Er core-NaLuF₄ shell NP@AzoPDMS/silk fibroin/AgNW nanocomposite film were independently and simultaneously operated by visible (Vis) to near-infrared (NIR) light as stimuli. Reversible switching between multistates allowed us to apply electrical stimulation with 400–700 nm light irradiation and monitor the device position in real-time with 980 nm light irradiation, respectively. We believe our photoresponsive multiswitch can broaden its application not only to remotely controlled electrical treatment but also biomedical devices for topical stimulation with restricted visibility and accessibility.

■ ASSOCIATED CONTENT

Data Availability Statement

The data sets used and/or analyzed during the current study are available from the corresponding author on reasonable request.

SI Supporting Information

The Supporting Information is available free of charge at <https://pubs.acs.org/doi/10.1021/acsami.3c08807>.

Photobending stability of the nanocomposite film determined by cyclic bending/stretching fatigue testing, ultraviolet–visible (UV–vis) absorption spectra of the nanocomposite film with cured AzoPDMS and uncured AzoPDMS prepolymer upon irradiation, time-resolved absorption (TA) spectra of the nanocomposite film with cured AzoPDMS and uncured AzoPDMS prepolymer, nuclear magnetic resonance (NMR) spectra of initial, *trans*-, and *cis*-prevailing AzoPDMS prepolymer, inductively coupled plasma-mass spectrometry (ICP-MS) data of NaYF₄:Yb,Er NPs and NaYF₄:Yb,Er core-NaLuF₄ shell NPs, transmission electron microscopy-energy dispersive spectroscopy (TEM-EDS) of NaYF₄:Yb,Er NPs and NaYF₄:Yb,Er core-NaLuF₄ shell NPs, particle concentration estimation of NP dispersion and the nanocomposite film, independent of PB and UCPL via light emission that is responsible for one another, variation of the excitation light power of each stimulus for controlling the bending degree of PB and emission intensity of UCPL, selective stimulation performance of the three films (Film 1, 2, and 3) from the nanocomposite film array demonstrates independent properties of UCPL and PB (PDF)

Video of the spatiotemporal switching process with a fixed nanocomposite film array on a brain model (Video S1) (MP4)

Video of spatiotemporal switching process with a mobile nanocomposite film on a nose model via NIR/Vis irradiation (Video S2) (MP4)

■ AUTHOR INFORMATION

Corresponding Authors

Sang-Yong Ju – Department of Chemistry, College of Science, Yonsei University, Seoul 03722, Republic of Korea;
✉ orcid.org/0000-0002-6939-5296; Email: syju@yonsei.ac.kr

Jiwon Kim – School of Integrated Technology, College of Computing, Yonsei University, Incheon 21983, Republic of Korea; Integrated Science and Engineering Division, Underwood International College and Integrative Biotechnology and Translational Medicine, Graduate School, Yonsei University, Incheon 21983, Republic of Korea;
✉ orcid.org/0000-0002-1458-4743; Email: jiwon.kim@yonsei.ac.kr

Authors

Jiyeon Lee – School of Integrated Technology, College of Computing, Yonsei University, Incheon 21983, Republic of Korea

Dongjun Kim – School of Integrated Technology, College of Computing, Yonsei University, Incheon 21983, Republic of Korea

Minsuk Park – Department of Chemistry, College of Science, Yonsei University, Seoul 03722, Republic of Korea

Jaehyeok Ryu – School of Integrated Technology, College of Computing, Yonsei University, Incheon 21983, Republic of Korea

Hyunbin Park – Integrative Biotechnology and Translational Medicine, Graduate School, Yonsei University, Incheon 21983, Republic of Korea

Taehee Kim – Department of Chemistry, College of Science, Yonsei University, Seoul 03722, Republic of Korea;
✉ orcid.org/0000-0001-9426-1006

Dongho Kim – Department of Chemistry, College of Science, Yonsei University, Seoul 03722, Republic of Korea;
✉ orcid.org/0000-0001-8668-2644

Complete contact information is available at:

<https://pubs.acs.org/doi/10.1021/acsami.3c08807>

Author Contributions

J.K., S.-Y.J., and D.K. supervised the project; J.L. performed the experimental work and wrote the manuscript with the support from all authors; D.K., M.P., and T.K. carried out photoluminescence measurements; J.R. performed the electrical switching test; D.K. and H.P. revised the manuscript. All authors discussed the results and contributed to the manuscript.

Notes

The authors declare no competing financial interest.

■ ACKNOWLEDGMENTS

This research was supported by the National Research Foundation of Korea (NRF) grants funded by the Korea Government (MSIT) (NRF-2020R1F1A107698311 and RS-2023-00240624) and the Ministry of Education (NRF-2021R1A6A3A13045892). This research was also supported by a grant (21CTAP-C157556-02) from the Technology Advancement Research Program (TARP) funded by the Ministry of Land, Infrastructure and Transport (MOLIT) of the Korea Government, and by Korea Institute of Energy Technology Evaluation and Planning (KETEP) grant funded by the Korea Government (MOTIE) (20201520300140, Development of Advanced Functional Material with C-14 from PHWR Waste). We would like to thank Yu Jin Lee of functional π -electronic system (FPIES) laboratory (Prof. Dongho Kim) at Yonsei University for her contribution to the time-resolved absorption experiments.

■ REFERENCES

- (1) Yuan, Q.; Zhang, Y.; Chen, T.; Lu, D.; Zhao, Z.; Zhang, X.; Li, Z.; Yan, C.-H.; Tan, W. Photon-Manipulated Drug Release from a Mesoporous Nanocontainer Controlled by Azobenzene-Modified Nucleic Acid. *ACS Nano* **2012**, *6* (7), 6337–6344.
- (2) Vivek, R.; Thangam, R.; Kumar, S. R.; Rejeeth, C.; Sivasubramanian, S.; Vincent, S.; Gopi, D.; Kannan, S. HER2 Targeted Breast Cancer Therapy with Switchable “Off/On” Multifunctional “Smart” Magnetic Polymer Core–Shell Nanocomposites. *ACS Appl. Mater. Interfaces* **2016**, *8* (3), 2262–2279.
- (3) Lin, X.; Nguyen Quoc, B.; Ulbricht, M. Magneto-responsive Poly(ether sulfone)-Based Iron Oxide cum Hydrogel Mixed Matrix Composite Membranes for Switchable Molecular Sieving. *ACS Appl. Mater. Interfaces* **2016**, *8* (42), 29001–29014.
- (4) Kim, S.; Byun, J.; Choi, S.; Kim, D.; Kim, T.; Chung, S.; Hong, Y. Negatively Strain-Dependent Electrical Resistance of Magnetically Arranged Nickel Composites: Application to Highly Stretchable Electrodes and Stretchable Lighting Devices. *Adv. Mater.* **2014**, *26* (19), 3094–3099.

- (5) Li, L.; Niu, R.; Zhang, Y. Ag–Au Bimetallic Nanocomposites Stabilized with Organic–Inorganic Hybrid Microgels: Synthesis and Their Regulated Optical and Catalytic Properties. *RSC Adv.* **2018**, *8* (22), 12428–12438.
- (6) Baek, S.; Singh, R. K.; Kim, T.-H.; Seo, J.-w.; Shin, U. S.; Chrzanowski, W.; Kim, H.-W. Triple Hit with Drug Carriers: pH- and Temperature-Responsive Theranostics for Multimodal Chemo- and Photothermal Therapy and Diagnostic Applications. *ACS Appl. Mater. Interfaces* **2016**, *8* (14), 8967–8979.
- (7) Guan, X.; Fan, K.; Gao, T.; Ma, A.; Zhang, B.; Song, J. A Novel Multi-Stimuli Responsive Gelator Based on D-Gluconic Acetal and its Potential Applications. *Chem. Commun.* **2016**, *52* (5), 962–965.
- (8) Xiong, J.; Wang, K.; Yao, Z.; Zou, B.; Xu, J.; Bu, X.-H. Multi-Stimuli-Responsive Fluorescence Switching from a Pyridine-Functionalized Tetraphenylethene AIEgen. *ACS Appl. Mater. Interfaces* **2018**, *10* (6), 5819–5827.
- (9) Zhang, M.; Wei, J.; Zhang, Y.; Bai, B.; Chen, F.; Wang, H.; Li, M. Multi-Stimuli-Responsive Fluorescent Switching Properties of Anthracene-Substituted Acylhydrazone Derivative. *Sens. Actuators, B* **2018**, *273*, 552–558.
- (10) Arumugaperumal, R.; Venkatesan, P.; Shukla, T.; Raghunath, P.; Singh, R.; Wu, S.-P.; Lin, M.-C.; Lin, H.-C. Multi-Stimuli-Responsive High Contrast Fluorescence Molecular Controls with a Far-Red Emitting BODIPY-Based [2] Rotaxane. *Sens. Actuators, B* **2018**, *270*, 382–395.
- (11) Dong, Y.; Wang, J.; Guo, X.; Yang, S.; Ozen, M. O.; Chen, P.; Liu, X.; Du, W.; Xiao, F.; Demirci, U.; Liu, B. F. Multi-Stimuli-Responsive Programmable Biomimetic Actuator. *Nat. Commun.* **2019**, *10*, No. 4087.
- (12) Wang, M.; Sayed, S. M.; Guo, L.-X.; Lin, B.-P.; Zhang, X.-Q.; Sun, Y.; Yang, H. Multi-Stimuli Responsive Carbon Nanotube Incorporated Polysiloxane Azobenzene Liquid Crystalline Elastomer Composites. *Macromolecules* **2016**, *49* (2), 663–671.
- (13) Yang, L.; Qi, K.; Chang, L.; Xu, A.; Hu, Y.; Zhai, H.; Lu, P. A Powerful Dual-Responsive Soft Actuator and Photo-to-Electric Generator Based on Graphene Micro-Gasbags for Bioinspired Applications. *J. Mater. Chem. B* **2018**, *6* (31), 5031–5038.
- (14) Pilz da Cunha, M.; Foelen, Y.; van Raak, R. J.; Murphy, J. N.; Engels, T. A.; Debije, M. G.; Schenning, A. P. An Untethered Magnetic- and Light-Responsive Rotary Gripper: Shedding Light on Photoresponsive Liquid Crystal Actuators. *Adv. Opt. Mater.* **2019**, *7* (7), No. 1801643.
- (15) Mishra, S.; Ashaduzzaman, M.; Mishra, P.; Swart, H. C.; Turner, A. P.; Tiwari, A. Stimuli-Enabled Zipper-Like Graphene Interface for Auto-Switchable Bioelectronics. *Biosens. Bioelectron.* **2017**, *89*, 305–311.
- (16) Pandeewar, M.; Senanayak, S. P.; Narayan, K.; Govindaraju, T. Multi-Stimuli-Responsive Charge-Transfer Hydrogel for Room-Temperature Organic Ferroelectric Thin-Film Devices. *J. Am. Chem. Soc.* **2016**, *138* (26), 8259–8268.
- (17) Bai, T.; Du, J.; Chen, J.; Duan, X.; Zhuang, Q.; Chen, H.; Kong, J. Reduction-Responsive Dithiomaleimide-Based Polymeric Micelles for Controlled Anti-Cancer Drug Delivery and Bioimaging. *Polym. Chem.* **2017**, *8* (46), 7160–7168.
- (18) Liu, X.; Liu, H.-J.; Cheng, F.; Chen, Y. Preparation and Characterization of Multi Stimuli-Responsive Photoluminescent Nanocomposites of Graphene Quantum Dots with Hyperbranched Polyethylenimine Derivatives. *Nanoscale* **2014**, *6* (13), 7453–7460.
- (19) Lee, J.; Lee, W.; Kim, D.; Kim, M.; Kim, J. Independent Multi-States of Photo-Responsive Polymer/Quantum Dot Nanocomposite Induced via Different Wavelengths of Light. *Sci. Rep.* **2019**, *9*, No. 12458.
- (20) Liu, Y.; Liang, S.; Yuan, C.; Best, A.; Kappl, M.; Koynov, K.; Butt, H. J.; Wu, S. Fabrication of Anticounterfeiting Nanocomposites with Multiple Security Features via Integration of a Photoresponsive Polymer and Upconverting Nanoparticles. *Adv. Funct. Mater.* **2021**, *31* (37), No. 2103908.
- (21) Choi, J.; Choi, M.-J.; Yoo, J.-K.; Park, W. I.; Lee, J. H.; Lee, J. Y.; Jung, Y. S. Localized Surface Plasmon-Enhanced Nanosensor Platform Using Dual-Responsive Polymer Nanocomposites. *Nanoscale* **2013**, *5* (16), 7403–7409.
- (22) Zhang, Y.; Chen, B.; Xu, S.; Li, X.; Zhang, J.; Sun, J.; Zheng, H.; Tong, L.; Sui, G.; Zhong, H.; et al. Dually Functionalized Core-Shell NaYF₄:Er³⁺/Yb³⁺@NaYF₄:Tm³⁺/Yb³⁺ Nanoparticles as Nano-Calorimeters and Nano-Thermometers for Advanced Photothermal Therapy. *Sci. Rep.* **2017**, *7*, No. 11849.
- (23) He, S.; Xia, H.; Zhang, J.; Zhu, Y.; Chen, B. Highly Efficient Up-Conversion Luminescence in Er³⁺/Yb³⁺ Co-Doped Na₃Lu₉F₃₂ Single Crystals by Vertical Bridgman Method. *Sci. Rep.* **2017**, *7*, No. 8751.
- (24) Janani, J.; Ramasubramanian, S.; Soni, A. K.; Rai, V. K.; Thiyagarajan, P. Luminescence Properties of LiYF₄:Yb³⁺, Er³⁺ Phosphors: A Study on Influence of Synthesis Temperature and Dopant Concentration. *Optik* **2018**, *169*, 147–155.
- (25) Liu, J.; Wu, S.; Chu, H.; Wang, C.; Shen, J.-W.; Wei, Y.; Wu, P. Low Power Density 980 nm-Driven Ultrabright Red-Emitting Upconversion Nanoparticles via Synergetic Yb³⁺/Tm³⁺ Cascade-Sensitization. *J. Mater. Chem. C* **2019**, *7* (43), 13415–13424.
- (26) Arumugam, G. M.; Xu, C.; Karunakaran, S. K.; Shi, Z.; Zhu, C.; Wei, M.; Feifei, Q. Efficient Red Up-Conversion Emission from Er³⁺-Yb³⁺ Co-Doped Rubidium Lead Iodide Perovskite Nanowires with Surface Plasmons. *Appl. Phys. Lett.* **2018**, *112* (5), No. 054104.
- (27) Zheng, W.; Huang, P.; Gong, Z.; Tu, D.; Xu, J.; Zou, Q.; Li, R.; You, W.; Bünzli, J.-C. G.; Chen, X. Near-Infrared-Triggered Photon Upconversion Tuning in All-Inorganic Cesium Lead Halide Perovskite Quantum Dots. *Nat. Commun.* **2018**, *9*, No. 3462.
- (28) Lee, W.; Kim, D.; Lim, J.; Kim, G.; Kim, I.; Kim, S.; Kim, J. Light-Induced Electrical Switch via Photo-Responsive Nanocomposite Film. *Sens. Actuators, B* **2018**, *266*, 724–729.
- (29) Luo, C.; Zuo, F.; Ding, X.; Zheng, Z.; Cheng, X.; Peng, Y. Light-Triggered Reversible Solubility of α -Cyclodextrin and Azobenzene Moiety Complexes in PDMAA-co-PAPA via Molecular Recognition. *J. Appl. Polym. Sci.* **2008**, *107* (4), 2118–2125.
- (30) Merino, E.; Ribagorda, M. Control Over Molecular Motion Using the Cis–Trans Photoisomerization of the Azo Group. *Beilstein J. Org. Chem.* **2012**, *8* (1), 1071–1090.
- (31) Li, B.; Wang, F.; Hu, F.; Ding, T.; Huang, P.; Xu, X.; Liang, J.; Li, C.; Zhou, Q.; Lu, M.; et al. Injectable “Nano-Micron” Combined Gene-Hydrogel Microspheres for Local Treatment of Osteoarthritis. *NPG Asia Mater.* **2022**, *14* (1), 1.
- (32) Yu, Y.; Nakano, M.; Ikeda, T. Directed Bending of a Polymer Film by Light. *Nature* **2003**, *425* (6954), 145.
- (33) Pang, X.; Qin, L.; Xu, B.; Liu, Q.; Yu, Y. Ultralarge Contraction Directed by Light-Driven Unlocking of Prestored Strain Energy in Linear Liquid Crystal Polymer Fibers. *Adv. Funct. Mater.* **2020**, *30* (32), No. 2002451.
- (34) Priimagi, A.; Shimamura, A.; Kondo, M.; Hiraoka, T.; Kubo, S.; Mamiya, J.-I.; Kinoshita, M.; Ikeda, T.; Shishido, A. Location of the Azobenzene Moieties within the Cross-Linked Liquid-Crystalline Polymers Can Dictate the Direction of Photoinduced Bending. *ACS Macro Lett.* **2012**, *1* (1), 96–99.
- (35) Marturano, V.; Ambrogio, V.; Bandeira, N.; Tylkowski, B.; Giamberini, M.; Cerruti, P. Modeling of Azobenzene-Based Compounds. *Phys. Sci. Rev.* **2019**, *2* (11), 1–12.
- (36) Zhang, L.; Liu, H.; Liu, Y.; Wu, Z. Thermodynamic Stability of Cis-Azobenzene Containing DNA Materials Based on Van Der Waals Forces. *Chem. Commun.* **2022**, *58* (23), 3811–3814.
- (37) Erekaht, S.; Chordiya, K.; Vidhya, K.; Kahaly, M. U.; Kalpathy, S. K. Self-Aggregation, H-Bonding, and Photoresponse in Film and Solution States of Azobenzene Containing Polyurea. *Phys. Chem. Chem. Phys.* **2022**, *24* (38), 23447–23459.
- (38) Homma, K.; Chang, A. C.; Yamamoto, S.; Ueki, T.; Nakanishi, J. Polarity Does Not Matter: Molecular Weight Reverses the Photoisomerization-Induced Phase Separation of an Azobenzene-Bearing Polymer. *Macromol. Rapid Commun.* **2023**, *44*, No. 2300118.
- (39) Bobrovsky, A.; Shibaev, V.; Cigl, M.; Hamplová, V.; Pocięcha, D.; Bubnov, A. Azobenzene-Containing LC Polymethacrylates Highly

Photosensitive in Broad Spectral Range. *J. Polym. Sci., Part A: Polym. Chem.* **2016**, *54* (18), 2962–2970.

(40) Li, M.; Zheng, J.; Wang, X.; Yu, R.; Wang, Y.; Qiu, Y.; Cheng, X.; Wang, G.; Chen, G.; Xie, K.; Tang, J. Light-Responsive Self-Strained Organic Semiconductor for Large Flexible OFET Sensing Array. *Nat. Commun.* **2022**, *13* (1), No. 4912.

(41) Tai, H.-T.; Lin, Y.-C.; Ma, J.-Y.; Lo, C.-T. Hydrogen Bonding-Induced Assembled Structures and Photoresponsive Behavior of Azobenzene Molecule/Polyethylene Glycol Complexes. *Polymers* **2019**, *11* (8), 1360.

(42) Giles, L. W.; Faul, C. F.; Tabor, R. F. Azobenzene Isomerization in Condensed Matter: Lessons for the Design of Efficient Light-Responsive Soft-Matter Systems. *Mater. Adv.* **2021**, *2* (13), 4152–4164.

(43) Freyer, W.; Brete, D.; Schmidt, R.; Gahl, C.; Carley, R.; Weinelt, M. Switching Behavior and Optical Absorbance of Azobenzene-Functionalized Alkanethiols in Different Environments. *J. Photochem. Photobiol.* **2009**, *204* (2–3), 102–109.

(44) Langley, D. *Silver Nanowire Networks: Effects of Percolation and Thermal Annealing on Physical Properties*. Ph.D. Thesis, Université de Grenoble, 2014.

(45) Nguyen, V. H.; Resende, J.; Papanastasiou, D. T.; Fontanals, N.; Jiménez, C.; Muñoz-Rojas, D.; Bellet, D. Low-Cost Fabrication of Flexible Transparent Electrodes Based on Al Doped ZnO and Silver Nanowire Nanocomposites: Impact of the Network Density. *Nanoscale* **2019**, *11* (25), 12097–12107.

(46) Wang, F.; Liu, X. Recent Advances in the Chemistry of Lanthanide-Doped Upconversion Nanocrystals. *Chem. Soc. Rev.* **2009**, *38* (4), 976–989.

(47) Heer, S.; Kömpe, K.; Güdel, H. U.; Haase, M. Highly Efficient Multicolour Upconversion Emission in Transparent Colloids of Lanthanide-Doped NaYF₄ Nanocrystals. *Adv. Mater.* **2004**, *16* (23–24), 2102–2105.

(48) Johnson, N. J. J.; van Veggel, F. C. Lanthanide-Based Heteroepitaxial Core–Shell Nanostructures: Compressive versus Tensile Strain Asymmetry. *ACS Nano* **2014**, *8* (10), 10517–10527.

(49) Zhou, D.; Liu, D.; Pan, G.; Chen, X.; Li, D.; Xu, W.; Bai, X.; Song, H. Cerium and Ytterbium Codoped Halide Perovskite Quantum Dots: A Novel and Efficient Downconverter for Improving the Performance of Silicon Solar Cells. *Adv. Mater.* **2017**, *29* (42), No. 1704149.

(50) Homann, C.; Krukewitt, L.; Frenzel, F.; Grauel, B.; Würth, C.; Resch-Genger, U.; Haase, M. NaYF₄:Yb, Er/NaYF₄ Core/Shell Nanocrystals with High Upconversion Luminescence Quantum Yield. *Angew. Chem., Int. Ed.* **2018**, *57* (28), 8765–8769.

(51) Han, Q.; Sun, J.; Wu, H.; Zou, Y.; Song, Y.; Wang, Y.; Zhang, X. Enhanced Up-Conversion Luminescence Efficiency of Heterogeneous Hetero-Phase α -NaLuF₄:Yb/Er@ β -NaYF₄:Yb Core-Shell Structure Nanocrystals. *J. Alloys Compd.* **2020**, *848*, No. 156543.

(52) Liu, Z. F.; Morigaki, K.; Enomoto, T.; Hashimoto, K.; Fujishima, A. Kinetic Studies on the Thermal Cis-Trans Isomerization of an Azo Compound in the Assembled Monolayer Film. *J. Phys. Chem. A* **1992**, *96* (4), 1875–1880.

(53) Kwon, Y.-b.; Kang, M.-s.; Ahn, C.-j.; Han, H.-j.; Ahn, B.-c.; Lee, J.-H. Effect of High or Low Frequency Electroacupuncture on the Cellular Activity of Catecholaminergic Neurons in the Brain Stem. *Acupunct. Electro-Ther. Res.* **2000**, *25* (1), 27–36.

(54) Du, S.; Zhou, N.; Gao, Y.; Xie, G.; Du, H.; Jiang, H.; Zhang, L.; Tao, J.; Zhu, J. Bioinspired Hybrid Patches with Self-Adhesive Hydrogel and Piezoelectric Nanogenerator for Promoting Skin Wound Healing. *Nano Res.* **2020**, *13*, 2525–2533.

(55) Wang, C.; Jiang, X.; Kim, H.-J.; Zhang, S.; Zhou, X.; Chen, Y.; Ling, H.; Xue, Y.; Chen, Z.; Qu, M.; et al. Flexible Patch with Printable and Antibacterial Conductive Hydrogel Electrodes for Accelerated Wound Healing. *Biomaterials* **2022**, *285*, No. 121479.

(56) Dong, M.; Babalhavaeji, A.; Samanta, S.; Beharry, A. A.; Woolley, G. A. Red-Shifting Azobenzene Photoswitches for in Vivo Use. *Acc. Chem. Res.* **2015**, *48* (10), 2662–2670.

(57) Carling, C.-J.; Boyer, J.-C.; Branda, N. R. Remote-Control Photoswitching Using NIR Light. *J. Am. Chem. Soc.* **2009**, *131* (31), 10838–10839.

Supporting Information

Spatiotemporally Controllable Electrical Stimulator via Independent Photobending and Upconversion Photoluminescence Using Two Different Wavelengths of Near-Infrared/Visible Light as Dual Stimuli

*Jiyeon Lee¹, Dongjun Kim¹, Minsuk Park², Jaehyeok Ryu¹, Hyunbin Park⁴, Taehee Kim²,
Dongho Kim², Sang-Yong Ju^{2,*} and Jiwon Kim^{1,3,4,*}*

¹ School of Integrated Technology, College of Computing, Yonsei University, 85
Songdogwahak-ro, Yeonsu-gu, Incheon, 21983, Republic of Korea.

² Department of Chemistry, College of Science, Yonsei University, 50 Yonsei-ro, Seodaemun-gu,
Seoul, 03722, Republic of Korea.

³ Integrated Science and Engineering Division, Underwood International College, Yonsei
University, 85 Songdogwahak-ro, Yeonsu-gu, Incheon, 21983, Republic of Korea.

⁴ Integrative Biotechnology and Translational Medicine, Graduate School, Yonsei University, 85 Songdogwahak-ro, Yeonsu-gu, Incheon, 21983, Republic of Korea.

* Corresponding Author E-mail: jiwon.kim@yonsei.ac.kr (Jiwon Kim); syju@yonsei.ac.kr (Sang-Yong Ju)

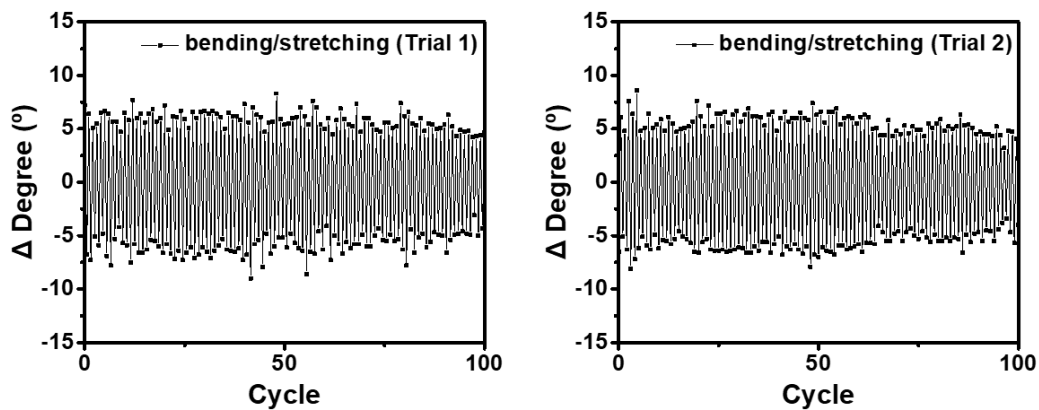


Figure S1. Photobending stability of nanocomposite film determined by cyclic bending/stretching fatigue testing. 2 trials are separated by 4 days, which indicates that the nanocomposite film not only maintains its properties without exhaustion even after 100 bending/stretching cycles, but also retains the same performance even after a few days.

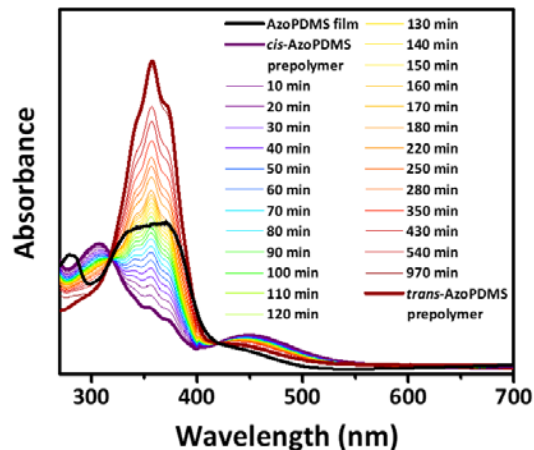


Figure S2. Changes in absorption spectrum of uncured AzoPDMS prepolymer upon irradiation.

The ultraviolet-visible (UV-Vis) absorption spectrum of AzoPDMS layer in the nanocomposite film was obtained upon irradiation of 365 nm and 400–700 nm for 1 hour, respectively (Fig. 2e). Upon irradiation of ultraviolet (UV) light (365 nm), absorption spectrum of AzoPDMS layer exhibited increase in peaks at 320 nm (π - π^* transition for *cis*-form) and 450 nm (n - π^* transition) corresponding to the *cis*-isomer indicating the film transited to *cis*-prevailing state compared to its initial state. On the other hand, when AzoPDMS layer was irradiated with visible (Vis) light (400–700 nm), the absorption spectrum exhibited increase in peak at 363 nm (π - π^* transition for *trans*-form) corresponding to the *trans*-isomer indicating the AzoPDMS layer transited to *trans*-prevailing state compared to its initial state. To note, the nanocomposite film returns to its initial state after the removal of light stimulus. This result indicates that the initial state of AzoPDMS layer in nanocomposite film is an intermediate state in between *trans*- and *cis*-prevailing states compared to AzoPDMS prepolymer as shown in the UV-Vis absorption spectra (Fig. S2).

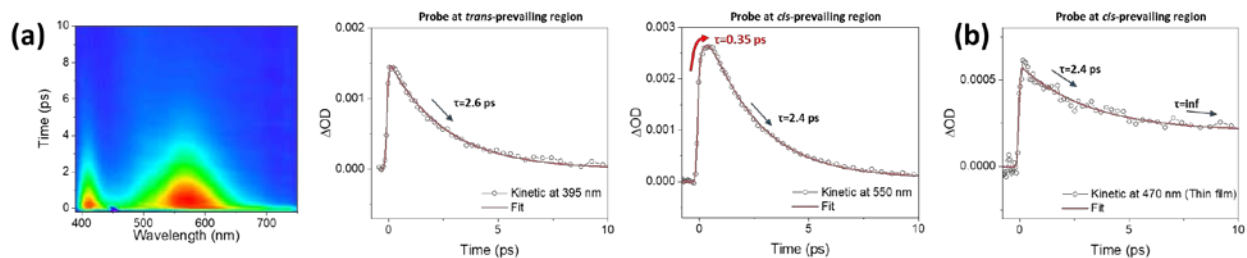


Figure S3. (a) TA spectra of AzoPDMS prepolymer (*left*), the decay profiles of *trans*- (*middle*; probe at 395 nm) and *cis*- (*right*; probe at 550 nm) prevailing region of AzoPDMS prepolymer upon excitation at 400 nm. (b) The decay profiles of *cis*-prevailing region (probe at 470 nm) of cured AzoPDMS upon excitation at 400 nm.

Time-resolved absorption (TA) spectroscopy data was obtained in order to observe the real-time changes in absorption during irradiation. TA spectrum encompasses ground state bleach (GSB), stimulated emission (SE), and excited-state absorption (ESA), with its profile undergoing modulation upon excitation by the incident wavelength¹. In addition, the probing wavelength offers insights into the temporal evolution of dynamics across electronic states. Therefore, we probed transition from *trans*- to *cis*-form of both AzoPDMS prepolymer (in toluene) and cured AzoPDMS via TA measurements initiated by 400 nm excitation, utilizing a flow cell for AzoPDMS prepolymer to avert photon accumulation. Specifically, real-time photoisomerization within *trans*-prevailing (probed at 395 nm) and *cis*-prevailing (probed at 550 nm) spectral regions were monitored (Fig. S3a). ESA signatures emanated from *trans*-azobenzene emerged at 360, 390, and 520 nm, while *cis*-azobenzene showcased peaks at 334 nm and 540 nm^{2,3}. These ESA patterns reveal plausible energy relaxation or isomerization pathways per electronic state. Notably, the kinetics at *cis*-prevailing realm exhibited a swift ascent in the ESA signal upon UV light irradiation, indicating *cis*-isomer emergence. In cured AzoPDMS, this trend was subdued (Fig. S3b), possibly owing to the modest divergence in the absorption spectrum between the *cis*- and *trans*-isomers

around the vicinity of 450 nm ($n-\pi^*$ transition for *cis*-form) – attributable to the stabilization at the intermediate state (Fig. 2e).

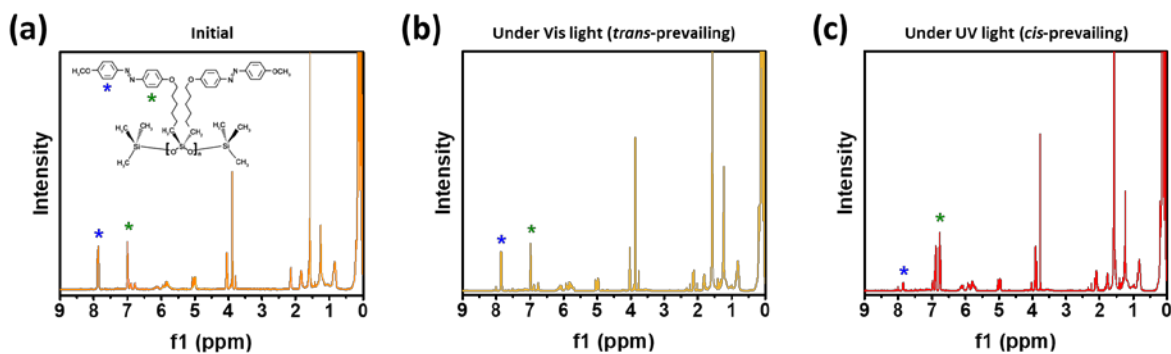


Figure S4. NMR spectra of (a) initial, (b) *trans*- and (c) *cis*-prevailing AzoPDMS prepolymer (dispersed in deuterated chloroform; CDCl₃).

Nuclear magnetic resonance (NMR) spectra of AzoPDMS prepolymer (dispersed in deuterated chloroform; CDCl₃) were obtained to examine the stability of each isomeric state – initial, *trans*-prevailing, and *cis*-prevailing states (Fig. S4)⁴. In the *trans*- and *cis*-prevailing AzoPDMS prepolymer, distinct patterns were observed in peaks corresponding to the two benzene rings (indicated by blue and green stars). The *cis*-AzoPDMS prepolymer exhibited a decrease in the intensity of the blue peak and an increase in the rightmost peak of the triplet corresponding to the green peak, relative to the *trans*-AzoPDMS prepolymer. This suggests that *cis*-AzoPDMS prepolymer contains a mixture of *trans*- and *cis*-isomers with remaining blue peak, which indicates the initial state would also have both isomers. The initial state of the AzoPDMS prepolymer displayed a *trans*-prevailing characteristic due to the absence of steric hindrance, as compared to the cured AzoPDMS state.

Table S1. Inductively coupled plasma-mass spectrometry (ICP-MS) data of NaYF₄:Yb,Er NPs and NaYF₄:Yb,Er core-NaLuF₄ shell NPs.

	Na (ppm)	Yb (ppm)	Er (ppm)	Lu (ppm)
NaYF ₄ :Yb,Er NPs	1870.566	17229.205	291.552	ND ^{a)}
Yb/Er ratio		98.3%	1.7%	
NaYF ₄ :Yb,Er core-NaLuF ₄ shell NPs	860.011	2229.505	36.899	5104.827
Yb/Er ratio		98.4%	1.6%	

a) ND: Not Detected.

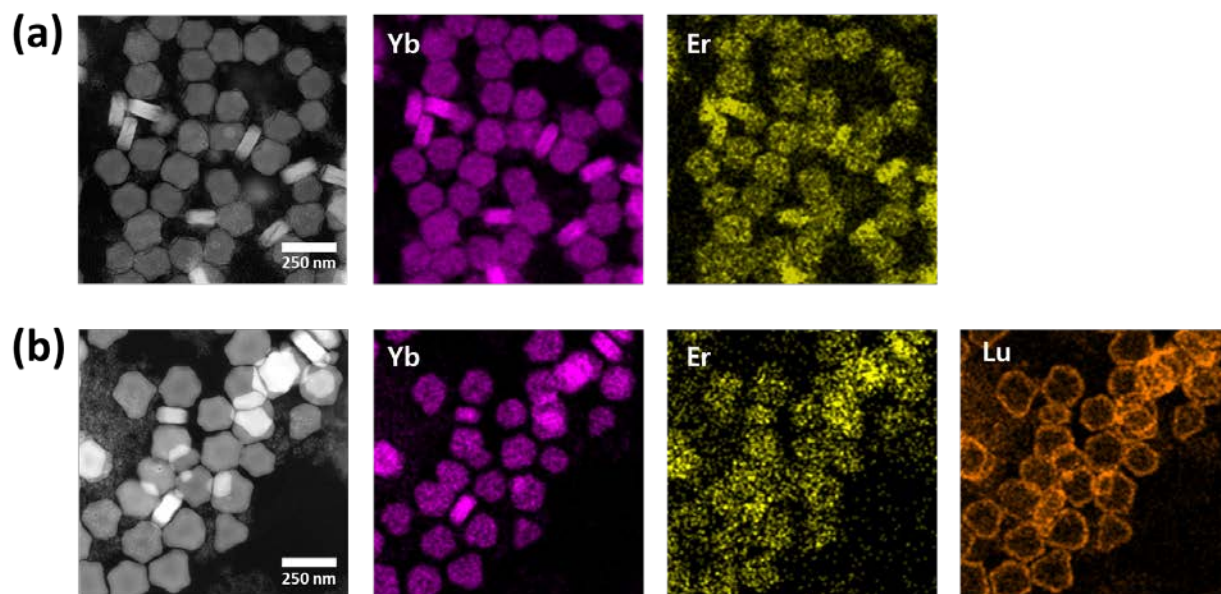


Figure S5. Transmission electron microscopy-energy dispersive spectroscopy (TEM-EDS) of (a) NaYF₄:Yb,Er NPs and (b) NaYF₄:Yb,Er core-NaLuF₄ shell NPs showing uniform doping of lanthanide ions – Yb³⁺ and Er³⁺ in core, and Lu³⁺ in shell.

Particle Concentration Estimation of NP dispersion and the nanocomposite film

The number of nanoparticles (NPs) per NP synthesis was calculated by the volume of NP and NaYF₄:Yb,Er unit cell (obtained from the PDF 28-1192 material used as a reference for X-ray diffraction (XRD)).

Volume of NP: $\frac{4}{3} \times \pi \times (12.2 \text{ nm})^3$ (radius based on NP size determined by TEM image in Fig. 3c, which is ~24.4 nm)

Volume of NaYF₄:Yb,Er Unit Cell: 107.977 \AA^3

Number of Unit Cell in One NP: Volume of NP / Volume of NaYF₄:Yb,Er Unit Cell = 70,442 particles

Assuming all the precursors are converted to NPs, 3 mmol (= 1.806×10^{21}) of NaYF₄:Yb,Er unit cells are synthesized from each NP synthesis, resulting in 2.564×10^{16} NPs.

Then, we can estimate the NP concentration in nanocomposite film by calculating the number of NPs used in nanocomposite film synthesis.

The NP dispersion was prepared by dispersing NPs in 15 mL of cyclohexane for measuring the concentration by UV-Vis spectroscopy, which yielded a concentration of NP as $\sim 1.710 \times 10^{15}$ particles/mL in the cuvette cell.

Since 0.4 mL of NaYF₄:Yb,Er NP solution was mixed with 1 g of AzoPDMS prepolymer followed by evaporation of the solvent (i.e., cyclohexane) for nanocomposite film synthesis, number of NPs in the 1 g of AzoPDMS can be estimated as below.

Number of NPs in the 1 g of AzoPDMS: $0.4 \text{ mL} \times 1.710 \times 10^{15} / 1 \text{ g} = 6.837 \times 10^{14}$ particles/g

Assuming that the density of AzoPDMS is similar to that of PDMS (0.965 g/mL), NP concentration in the nanocomposite film can be estimated as follows:

NP concentration in the nanocomposite film: $6.837 \times 10^{14} \text{ particles/g} \times 0.965 \text{ g/mL} = 6.598 \times 10^{14}$ particles/mL

In addition, the pathlength of the beam in UV-Vis measurement for NP dispersion and nanocomposite film is 10 mm (the thickness of the cuvette cell) and 10.09 μm (the thickness of the AzoPDMS in the nanocomposite film; measured from SEM cross-section image in Fig. 1c), respectively.

Therefore, number of NPs absorbing light is determined as below for both NP dispersion and nanocomposite film, where A denotes for the width of the light beam.

Number of NPs in the NP dispersion in cuvette cell: 1.710×10^{15} particles/mL \times 10 mm \times A

Number of NPs in the nanocomposite film: 6.598×10^{14} particles/mL \times 10.09 μm \times A

Ratio of number of NPs in the NP dispersion and the nanocomposite film: ~ 2569

Thus, the number of NPs that absorb light when traveling through the dispersion is ~ 2569 times higher than that of the nanocomposite film.

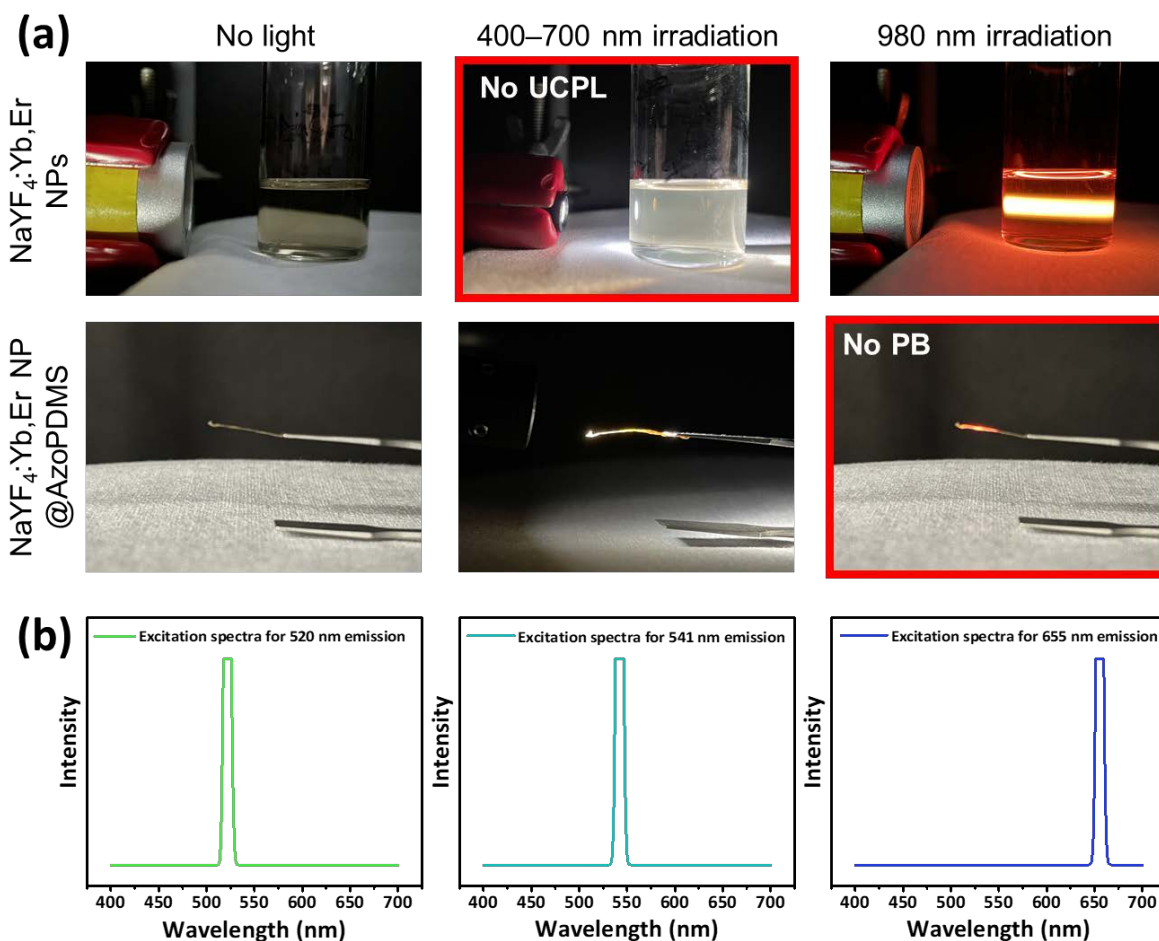


Figure S6. Independence of PB and UCPL via light emission that is responsible for one another.

(a) Optical images of NaYF₄:Yb,Er NPs and NaYF₄:Yb,Er core-NaLuF₄ shell NP@AzoPDMS nanocomposite film in response to no light, and irradiation using 400–700 nm or 980 nm light. (b) Fluorescence excitation spectra of NaYF₄:Yb,Er core-NaLuF₄ shell NP@AzoPDMS nanocomposite film indicating absence of excitation peaks at 400–700 nm range, except at the wavelength equivalent to the excitation light source.

The onset of PB and UCPL occur independently upon specific wavelengths of light, in which the wavelengths do not interfere with the activation of the other property. Fig. S6a shows the independence of

PB and UCPL by demonstrating that 400–700 nm light irradiation did not cause UCPL in the embedded NaYF₄:Yb,Er core-NaLuF₄ shell NPs, while 980 nm light did not induce PB of the nanocomposite film. Moreover, we scanned the excitation light from 400 to 700 nm with peaks of interest fixed at 520, 541, and 655 nm (Fig. S6b) to determine the excitation wavelength responsible for the observed UCPL peaks. Each spectrum exhibited a single peak at a wavelength equivalent to the excitation light source due to the direct detection by the emission detector. Since no other peaks were identified, we presume that visible light of 400–700 nm is independent of UCPL.

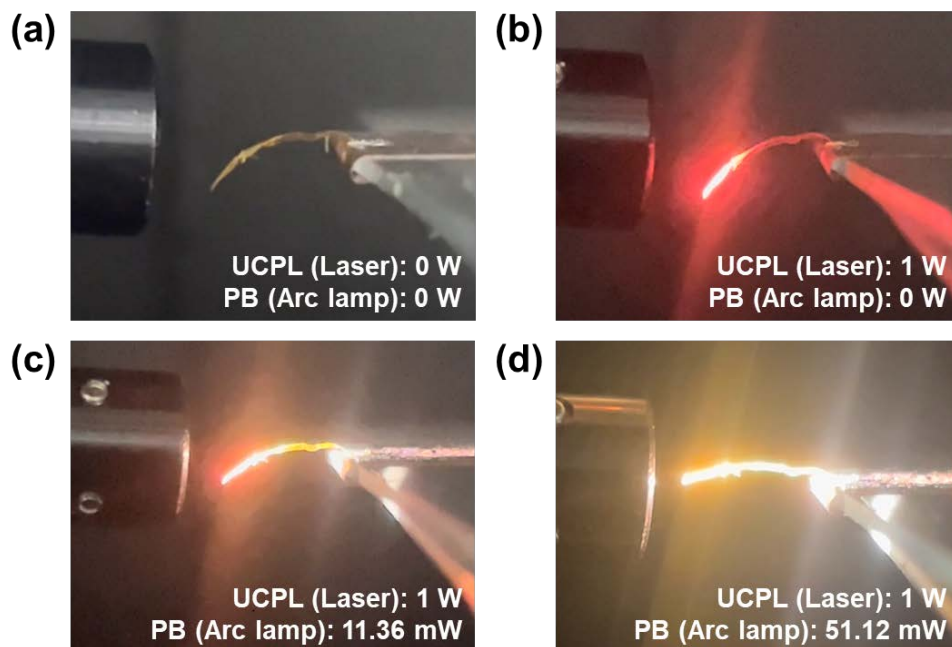


Figure S7. Variation of the excitation light power of each stimulus for controlling the bending degree of PB and emission intensity of UCPL; (a) No UCPL and PB upon absence of 980 nm (laser) and 400–700 nm (arc lamp) irradiation, (b) UCPL upon 980 nm light (1 W), (c) UCPL and PB with less bending degree upon 980 nm light (1 W) and 400–700 nm light (11.36 mW), and (d) UCPL and PB with more bending degree upon 980 nm light (1 W) and 400–700 nm light (51.12 mW). Obscurement of UCPL emission by the light source (i.e., arc lamp) for PB could be reduced by regulating the lamp’s relative intensity.

Video S1. Spatio-temporal switching process with fixed nanocomposite film array on a brain model via NIR/Vis irradiation.

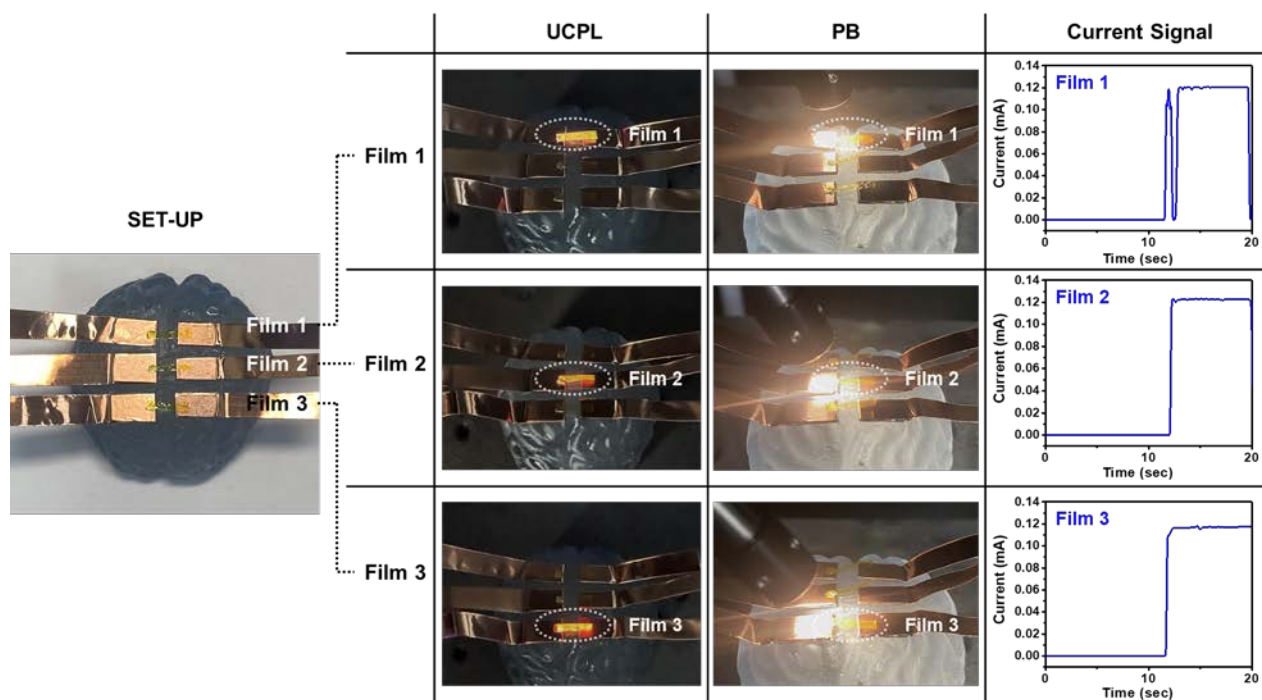


Figure S8. The selective stimulation performance of the three films (Film 1, 2, and 3) from the nanocomposite film array demonstrates independent properties of UCPL and PB. The current signal corresponds to the PB-activated conductance, where each film is connected to a separate electrode.

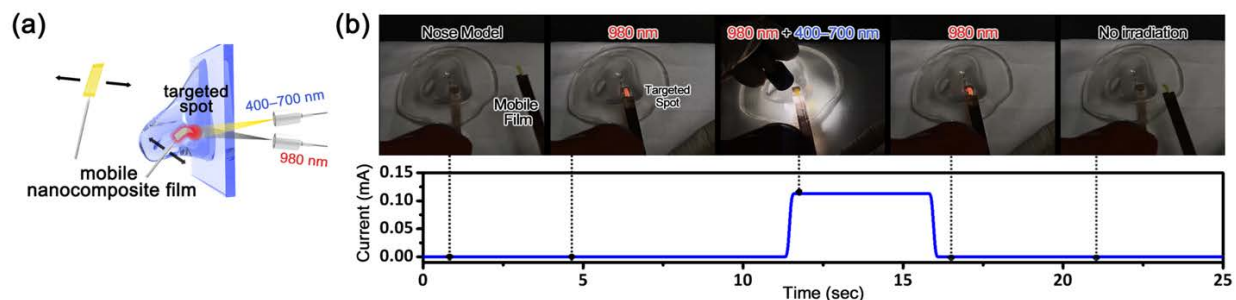


Figure S9. (a) Schematic images of a nanocomposite film as a spatio-temporally controllable electrical stimulator demonstrated with mobile nanocomposite film on a nose model via NIR/Vis irradiation. (b) The nanocomposite film operating the sequential process of location monitoring and electrical stimulation via NIR/Vis irradiation placing a mobile nanocomposite film with an electrical circuit on a nose model.

To precisely locate and stimulate the targeted area, a spatio-temporally controlled electrical stimulator composed of nanocomposite film was also employed as an electrocautery tip. Detailedly, the position of the mobile nanocomposite film was determined by exposure of fixed 980 nm light to the implanted electrode at the desired location, triggering UCPL emission from the film upon arrival. Subsequent irradiation with 400–700 nm light enabled targeted electrical stimulation via contact between nanocomposite film and implanted electrode through PB. The demonstration as a light-induced electrical stimulator was conducted in the similar process of location detection and electrical stimulation as previously described in Fig. 4c; i) an initial state with no irradiation was observed, ii) followed by detection of UCPL by fixed 980 nm light irradiation as the film approach to the target spot, iii) then 400–700 nm light was added for simultaneous UCPL and PB, iv) and 400–700 nm light was removed afterwards to stop stimulating, and v) finally the film was moved out. This experimental process is illustrated at the top of Fig. S9b and the corresponding current graph is presented below. A video of the full process is available in the Supporting Information (Video S2). The delays in OFF→ON (1.5 sec) and

ON→OFF (1.0 sec) states are owing to the required actuation time for contact between the film and the electrode as explained in Fig. 2h. Our nanocomposite film not only treated hard-to-reach areas with its precise adhesion, but also protected adjacent areas from damage with its one-sided conductivity. This effectively addresses the limitations of existing electrocautery techniques, which are susceptible to burning caused by small electrode sizes, limited contact, and application to unintended locations.

Video S2. Spatio-temporal switching process with mobile nanocomposite film on a nose model via NIR/Vis irradiation.

REFERENCES

- (1) Zhang, Q.; Luo, Y. Probing the Ultrafast Dynamics in Nanomaterial Complex Systems by Femtosecond Transient Absorption Spectroscopy. *High Power Laser Sci. Eng.* 2016, 4, e22.
- (2) Quick, M.; Dobryakov, A.; Gerecke, M.; Richter, C.; Berndt, F.; Ioffe, I.; Granovsky, A.; Mahrwald, R.; Ernsting, N.; Kovalenko, S. Photoisomerization Dynamics and Pathways of Trans-and Cis-Azobenzene in Solution from Broadband Femtosecond Spectroscopies and Calculations. *J. Phys. Chem. B* 2014, 118 (29), 8756-8771.
- (3) Sartin, M. M.; Osawa, M.; Takeuchi, S.; Tahara, T. Ultrafast Dynamics of an Azobenzene-Containing Molecular Shuttle Based on a Rotaxane. *Chem. Commun.* 2022, 58 (7), 961-964.
- (4) Constantin, C.-P.; Sava, I.; Damaceanu, M.-D. Structural Chemistry-Assisted Strategy toward Fast Cis–Trans Photo/Thermal Isomerization Switch of Novel Azo-Naphthalene-Based Polyimides. *Macromolecules* 2021, 54 (3), 1517-1538.